Available online at www.sciencedirect.com
SCIENCE DIRECT®
Journal of Computational Physics 216 (2006) 52–75
JOURNAL OF COMPUTATIONAL PHYSICS
www.elsevier.com/locate/jcp

Multiscale simulations for suspensions of rod-like molecules

Christiane Helzel *, Felix Otto

Institut für Angewandte Mathematik, Universität Bonn, Wegelerstr. 6 and 10, 53115 Bonn, Germany

Received 5 July 2005; received in revised form 11 November 2005; accepted 17 November 2005
Available online 4 January 2006

Abstract

We study the Doi model for suspensions of rod-like molecules. The Doi model couples a *microscopic* Fokker–Planck type equation (Smoluchowski equation) to the *macroscopic* Stokes equation. The Smoluchowski equation describes the evolution of the distribution of the rod orientations; it comes as a drift–diffusion equation on the sphere at every point in physical space.

For sufficiently high macroscopic shear rates (high Deborah numbers), the solution of the coupled system develops internal layers in the macroscopic strain rate (the spurt phenomenon).

In the high Deborah numbers regime, the drift term in the Smoluchowski equation is dominant. We thus introduce a finite-volume type discretization of the microscopic Smoluchowski equation which is motivated by transport-dominated PDEs.

We carry out direct numerical simulations of the spurt phenomenon both in the dilute and concentrated regimes. Below the isotropic–nematic transition, the solution structure is identical to the one described by purely macroscopic models (JSO model). For higher concentrations, we observe the formation of microstructure coming from a position-dependent tumbling rate. We also investigate the 2-d stability of the spurted solution.

Keywords: Rod-like molecules; Viscoelastic material; Spurt

1. Introduction

Many fluids are viscoelastic materials in the sense that the stress exposed to a macroscopic fluid element depends on the history of the deformation experienced by that element. The rheological properties of viscoelastic liquids are governed by the flow-induced evolution of molecular configurations. Thus a detailed mathematical model of viscoelastic flow problems requires a description of *microscopic* (or mesoscopic) molecular orientations and *macroscopic* rheological response.

In this paper, the macroscopic flow is described by the Stokes equations, which model a creeping flow where inertial effects are negligible (zero Reynolds number limit of the Navier–Stokes equation). Our microscopic model is a kinetic equation for the orientation of rigid rods which are assumed to have the same length. This

* Corresponding author. Tel.: +49 228 733420.
E-mail addresses: helzel@iam.uni-bonn.de (C. Helzel), otto@iam.uni-bonn.de (F. Otto).

0021-9991/$ - see front matter
doi:10.1016/j.jcp.2005.11.028

results in the so-called *Smoluchowski equation*, a Fokker–Planck equation on the sphere. The macroscopic flow model is coupled to the microscopic description of rod orientations via an elastic stress (arising as an additional term in the Stokes equations). The drift term in the microscopic Smoluchowski equation depends on the macroscopic velocity gradient of the flow. Besides the interaction with the flow, in the concentrated regime an interaction between molecules is modeled. Furthermore, the rods are subject to Brownian forces. A mathematical description of the models considered in this paper is given in Section 2. These models were derived by Doi and Edwards [4]. Note that by using a coupled micro–macro model we avoid possible inaccuracies due to closure approximations.

Here, we are interested in the development of appropriate numerical methods. This is quite challenging due to the high dimensionality of the problem. The coupled problem is a pde in 5 dimensions plus time: the distribution of rod orientations is monitored in every point of physical space. In the calculations shown in this paper, we restrict our considerations to geometries with spatial symmetries where the physical space is effectively 2-dimensional, this leads to a pde in 4 dimensions. The coupled problem shows interesting phenomena, in particular the spurt phenomenon. Spurt describes a sudden increase of the volumetric flow rate at a critical stress which has also been observed experimentally, see for instance Vinogradov et al. [31]. In [18], this was connected with the occurrence of internal layers, across which the shear rate is nearly discontinuous. For our model spurt can be observed in the high Deborah number regime, this was recently analyzed in [24]. In order to observe a correct prediction of the spurt phenomenon in numerical simulations, we develop a numerical method that leads to accurate results in the high Deborah number regime. We are not aware of other numerical simulations where a spurt solution was approximated for a coupled micro–macro model of viscoelastic fluids.

During the last decades, most of the numerical methods for viscoelastic fluids were developed for purely macroscopic models. In those models, the momentum and continuity equations are equivalent to our model but the elastic stress is modeled by a constitutive equation, see for instance Joseph [6] for a large variety of models. The macroscopic Johnson–Segalman–Oldroyed (JSO) model also predicts the spurt phenomenon. In a series of papers Malkus, Nohel, Pego, Plohr and Tzavaras have studied this model both analytically and numerically, see [18–20,22,23]. We found that in the dilute regime the steady-state solution structure for shear flow, obtained by our micro–macro model, agrees with the solution structure predicted by the JSO model, this will be discussed in some more detail in Section 4. Furthermore, we show numerical calculations for the multiscale shear flow problem in the concentrated regime. In this case, we also observe the spurt phenomenon. However, the spurt solutions in the concentrated regime develop a fine scale substructure, see Section 5.

In a recent review paper, Keunings [9] gives an overview about the current state of the art of micro–macro models for viscoelastic fluids and their numerical treatment. Most kinetic models for polymer solutions are based on dumbbell models. The CONNFFESSIT method introduced by Laso and Öttinger [12] has had a significant impact on the development of micro–macro techniques. This approach uses Monte-Carlo methods for the approximation of an equivalent stochastic differential equation of the kinetic model. Jourdain et al. [8] show that in a simple shear flow situation their numerical micro–macro model (a finite element method coupled to a Monte-Carlo method) converges to the exact solution. In their work, a dumbbell model was used to describe the microscopic behavior. Control of variance is the major issue in stochastic micro–macro simulations, see Jourdain et al. [7]. This problem does not arise in direct numerical simulations of the Fokker–Planck equation. However, simulations of the Fokker–Planck equation seem to be feasible only for microscopic models with relatively few configurational degrees of freedom. So far most of the Fokker–Planck simulations have been performed for models of rod-like polymers. Typically, the numerical approximation of the distribution function of rod orientations is based on a Galerkin Ansatz using spherical harmonics. Since spherical harmonics are the eigenfunctions of the Laplace operator on the sphere, this choice of basis functions is expected to be optimal in the diffusion-dominated case of small deformation rates, i.e. in the small Deborah number regime. Detailed numerical simulations of the uncoupled Smoluchowski equation have lead to a good understanding of the complex dynamic behavior of rod-like polymers under shear flow, see Marrucci and Maffettone [21], Larson [10], Larson and Öttinger [11], Fafaoni et al. [5]. We will present some test calculations in Section 3.6. However, in order to simulate the spurt phenomenon we need a numerical method that is accurate in the advection-dominated regime of large Deborah number. For this, we use a variant of LeVeque's wave

propagation algorithm [15]. We have developed a method for advective transport (with spatially varying velocity field) on the sphere that is a generalization of the recently suggested *f*-wave approach [2] for hyperbolic problems with spatially varying flux function, see Section 3.

The proposed algorithm for the microscopic solution structure, describing the rod orientation on the sphere, has been implemented as an extension of the CLAWPACK (Conservation LAW PACKage) software by LeVeque [13] which is freely available on the web. We have extended the software to the case of advection–diffusion problems on the sphere. This should be of use also for several other applications. The source code developed for the Smoluchowski equation can be obtained via the web at http://www.iam.uni-bonn.de/~helzel/smoluchowski.

2. The mathematical multiscale model

We consider liquid crystal molecules that assume a rigid rod-like structure. Let L be the constant length of the rod-like molecules and b their thickness. We consider slender rods, i.e. we assume $b \ll L$. Furthermore, let ν denote the constant number density of the rod-like molecules. Following Doi and Edwards [4], we distinguish three regimes:

Dilute regime. The rods are well separated, as expressed by $\nu \ll L^{-3}$, i.e. the averaged distance between polymers is much larger than L.

Concentrated regime. The excluded volume effects reduce the entropy substantially. The theory by Onsager shows that this happens for $\nu \gtrsim b^{-1}L^{-2}$. Polymers tend to orient in the same direction as their neighbors. For a critical value of the dimensionless number $\nu b L^2$, this leads to isotropic nematic phase transition.

Semi-dilute regime. On one hand, there is the kinetic effect that rods hinder themselves in their rotational movement. On the other hand, there is not yet an entropic effect: $L^{-3} \ll \nu \ll b^{-1}L^{-2}$.

For all three regimes Doi and Edwards [4] introduced kinetic models. See also [24] for a derivation of the equations in the form used here.

The microscopic system is described by a local probability distribution $\psi(t,\vec{x},\vec{n})\,\mathrm{d}\vec{n}$. It gives the time-dependent probability that a rod with center of mass at $\vec{x}$ has an axis in the area element $\mathrm{d}\vec{n}$. The relations

$$\psi \geqslant 0 \quad \text{and} \quad \int_{S^2} \psi \,\mathrm{d}\vec{n} = 1 \tag{1}$$

hold for all times.

In the *dilute regime*, the evolution of ψ is given by the Smoluchowski equation

$$\partial_t \psi(t,\vec{x},\vec{n}) + \vec{u}(t,\vec{x}) \cdot \nabla_{\vec{x}} \psi(t,\vec{x},\vec{n}) + \nabla_{\vec{n}} \cdot (P_{\vec{n}^\perp} \nabla_{\vec{x}} \vec{u}(t,\vec{x}) \vec{n} \psi(t,\vec{x},\vec{n})) = D_\mathrm{r} \nabla_{\vec{n}}^2 \psi(t,\vec{x},\vec{n}). \tag{2}$$

Here the second term describes advection of the centers of mass by the macroscopic velocity $\vec{u}$, the third term describes the rotation of the axis due to a velocity gradient $\nabla_{\vec{x}}\vec{u}$ and the term on the right-hand side models rotational diffusion due to Brownian motion. Here $P_{\vec{n}^\perp}\nabla_{\vec{x}}\vec{u}\vec{n} := \nabla_{\vec{x}}\vec{u}\vec{n} - (\vec{n}\cdot\nabla_{\vec{x}}\vec{u}\vec{n})\vec{n}$ denotes the projection of the vector $\nabla_{\vec{x}}\vec{u}\vec{n}$ on the tangent space in $\vec{n}$. Gradient, divergence and Laplacian on the unit sphere are denoted by $\nabla_{\vec{n}}$, $\nabla_{\vec{n}}\cdot$ and $\nabla_{\vec{n}}^2$, while gradient and divergence in physical space are denoted by $\nabla_{\vec{x}}$ and $\nabla_{\vec{x}}\cdot$.

A velocity gradient $\nabla_{\vec{x}}\vec{u}$ distorts an isotropic distribution ψ which leads to an increase in entropy. Thermodynamic consistency [4, Section 8.6] requires that this is balanced by a stress tensor $\sigma(t,\vec{x})$ given by

$$\sigma(t,\vec{x}) := \int_{S^2} (3\vec{n}\otimes\vec{n} - \mathrm{id})\psi(t,\vec{x},\vec{n})\,\mathrm{d}\vec{n}. \tag{3}$$

Here, σ plays the role of an elastic stress arising as additional term in the Stokes equation that models the macroscopic flow. The averaged momentum and continuity equations take the form

$$\nabla_{\vec{x}} \cdot \left(\left(\nabla_{\vec{x}}\vec{u}(t,\vec{x}) + \nabla_{\vec{x}}^t \vec{u}(t,\vec{x}) \right) - p(t,\vec{x})\mathrm{id} + \sigma(t,\vec{x}) \right) = -\vec{F}_{\mathrm{ext}}(t,\vec{x}), \tag{4}$$

$$\nabla_{\vec{x}} \cdot \vec{u}(t,\vec{x}) = 0, \tag{5}$$

where $\vec{u}$ is the macroscopic velocity, p the pressure and $\vec{F}_{\mathrm{ext}}$ is an externally imposed volume force. Note that the time evolution of the flow is governed entirely by the time dependence of the forces $\vec{F}_{\mathrm{ext}}$ and the time dependence of the elastic stress σ.

In the *semi-dilute regime*, rotational motion of a rod is hindered by the presence of the other rods. Within a mean field framework, a rod with axis $\vec{n}$ and center of mass $\vec{x}$ feels a rotational diffusivity $D_r(t,\vec{x},\vec{n})$ which depends on $\psi(t,\vec{x},\vec{n}')\,d\vec{n}'$. Modeling based on a tube concept [4, Section 9.2] leads to the expression

$$D_r(t,\vec{x},\vec{n}) := D_{r,dil}\left(\frac{4}{\pi}\int_{S^2}|\vec{n}\times\vec{n}'|\psi(t,\vec{x},\vec{n}')\,d\vec{n}'\right)^{-2}, \tag{6}$$

where $D_{r,dil}$ is the rotational diffusivity in a hypothetical isotropic solution of molecules at the given concentration. With this model, motion perpendicular to the polymer is severely limited by surrounding polymers.

Instead of (6) an averaged quantity

$$\bar{D}_r(t,\vec{x}) := D_{r,dil}\left(\frac{4}{\pi}\int_{S^2}\int_{S^2}|\vec{n}\times\vec{n}'|\psi(t,\vec{x},\vec{n})\psi(t,\vec{x},\vec{n}')\,d\vec{n}\,d\vec{n}'\right)^{-2} \tag{7}$$

may be used. Although the averaging removes the dependence on $\vec{n}$, a dependence on the average degree of molecular orientation is retained. The higher the degree of orientation, the less the molecules hinder each others rotational motion and the larger $\bar{D}_r(t,\vec{x})$ becomes. The elastic stress is again calculated by Eq. (3) and the same momentum and continuity equations (4) and (5) are used to update the macroscopic flow field.

In the *concentrated regime* excluded volume effects occur. The presence of a rod with axis $\vec{n}$ reduces the phase space volume for rods with axis $\vec{n}'$. The Smoluchowski equation which now models the evolution of the distribution function in the presence of flow and excluded volume effects has the form

$$\partial_t\psi + \vec{u}\cdot\nabla_{\vec{x}}\psi + \nabla_{\vec{n}}\cdot(P_{\vec{n}^\perp}\nabla_{\vec{x}}\vec{u}\vec{n}\psi) = D_r\left(\nabla_{\vec{n}}^2\psi + \nabla_{\vec{n}}\cdot(\psi\nabla_{\vec{n}}V_{ev})\right). \tag{8}$$

Here D_r is the orientation-independent rotational diffusion constant, and V_{ev} is an excluded volume potential. We will use the Maier–Saupe excluded volume potential:

$$V_{ev}(\vec{n}) := U\int_{S^2}|\vec{n}\times\vec{n}'|^2\psi(\vec{n}')\,d\vec{n}', \tag{9}$$

with the dimensionless parameter $U := 2vbL^2$. The elastic stress tensor takes the form:

$$\sigma(\vec{x},t) := \int_{S^2}((3\vec{n}\otimes\vec{n}-\mathrm{id})\psi + (\nabla_{\vec{n}}V_{ev}\otimes\vec{n})\psi)\,d\vec{n}. \tag{10}$$

To gain understanding of the microscopic solution structure, we will study solutions of the Smoluchowski equation for an externally given velocity field $\nabla_{\vec{x}}\vec{u}_{ext}$. The number $De := |\nabla_{\vec{x}}\vec{u}_{ext}|/D_r$ which relates the externally exposed time scale to the time scale related to rotational diffusion is called the *Deborah number*.

3. A numerical method for the Smoluchowski equation

In this section, we describe our numerical method for the discretization of the Smoluchowski equation on the sphere, i.e. both on S^1 and S^2, at a fixed point in physical space assuming that a constant externally imposed velocity gradient $\nabla_{\vec{x}}\vec{u}_{ext}$ is given. We first consider the dilute regime, i.e. we want to approximate

$$\partial_t\psi + \nabla_{\vec{n}}\cdot(P_{\vec{n}^\perp}\nabla_{\vec{x}}\vec{u}_{ext}\vec{n}\psi) - D_r\nabla_{\vec{n}}^2\psi = 0 \tag{11}$$

with given initial values $\psi(t_0,\vec{n})$ that satisfy $\int_{S^2}\psi(t_0,\vec{n})\,d\vec{n} = 1$. Here, we propose an algorithm that fits well into the multidimensional wave propagation concept of the CLAWPACK software. Our discretization is based on a formulation of the Smoluchowski equation in spherical coordinates.

3.1. The Smoluchowski equation in spherical coordinates

We are mostly interested in an externally imposed velocity gradient which comes from a shear flow:

$$\nabla_x\vec{u}_{ext} = \begin{pmatrix} u_{11} & u_{12} & u_{13}\\ u_{21} & u_{22} & u_{23}\\ u_{31} & u_{32} & u_{33}\end{pmatrix} = \begin{pmatrix} 0 & 1 & 0\\ 0 & 0 & 0\\ 0 & 0 & 0\end{pmatrix}.$$

Here, we have chosen the Cartesian coordinates such that

first component $\hat{=}$ flow direction

second component $\hat{=}$ shear direction

third component $\hat{=}$ vorticity direction.

Our numerical method will be based on spherical coordinates. It is convenient to put the poles into the vorticity direction: In this case, the drift velocity

$$\vec{b} = P_{\vec{n}^\perp} \nabla_{\vec{x}} \vec{u}_{\text{ext}} \vec{n}$$

vanishes at the poles.

To be more specific, we write

$$\vec{n} = \begin{pmatrix} \cos\phi \sin\theta \\ \sin\phi \sin\theta \\ -\cos\theta \end{pmatrix}, \quad \vec{e}_\phi = \frac{1}{\sin\theta} \frac{\partial \vec{n}}{\partial \phi} = \begin{pmatrix} -\sin\phi \\ \cos\phi \\ 0 \end{pmatrix}, \quad \vec{e}_\theta = \frac{\partial \vec{n}}{\partial \theta} = \begin{pmatrix} \cos\phi\cos\theta \\ \sin\phi\cos\theta \\ \sin\theta \end{pmatrix}.$$

with $\phi \in [0, 2\pi]$ and $\theta \in [0, \pi]$. Notice that $\{\vec{n}, \vec{e}_\phi, \vec{e}_\theta\}$ is an orthonormal basis of $\mathbb{R}^3$ and thus $\{\vec{e}_\phi, \vec{e}_\theta\}$ an orthonormal basis of the tangent space of S^2 at $\vec{n}$. We decompose the drift velocity accordingly

$$\vec{b} = b_\phi \vec{e}_\phi + b_\theta \vec{e}_\theta \quad \text{with } b_\phi = \vec{b} \cdot \vec{e}_\phi, \;\; b_\theta = \vec{b} \cdot \vec{e}_\theta, \tag{12}$$

and notice that for a function on S^2

$$\nabla_{\vec{n}} \zeta = \frac{1}{\sin\theta} \partial_\phi \zeta \vec{e}_\phi + \partial_\theta \zeta \vec{e}_\theta. \tag{13}$$

Finally, we recall that the area element $\mathrm{d}\vec{n}$ on S^2 transforms according to

$$\mathrm{d}\vec{n} = \left| \frac{\partial \vec{n}}{\partial \phi} \times \frac{\partial \vec{n}}{\partial \theta} \right| \mathrm{d}\phi \, \mathrm{d}\theta = \sin\theta |\vec{e}_\phi \times \vec{e}_\theta| \, \mathrm{d}\phi \, \mathrm{d}\theta = \sin\theta \, \mathrm{d}\phi \, \mathrm{d}\theta. \tag{14}$$

This information is used to derive the Smoluchowski equation in spherical coordinates, passing via the weak formulation:

$$\begin{aligned}
0 &= \int_{S^2} (\partial_t \psi + \nabla_{\vec{n}} \cdot (b\psi) - D_\mathrm{r} \nabla^2_{\vec{n}} \psi) \zeta \, \mathrm{d}\vec{n} \\
&= \int_{S^2} (\zeta \partial_t \psi - \psi b \cdot \nabla_{\vec{n}} \zeta + D_\mathrm{r} \nabla_{\vec{n}} \psi \cdot \nabla_{\vec{n}} \zeta) \, \mathrm{d}\vec{n} \\
&\overset{(12)\text{–}(14)}{=} \int_0^\pi \int_0^{2\pi} \left\{ \zeta \partial_t \psi - \psi \left(\frac{1}{\sin\theta} b_\phi \partial_\phi \zeta + b_\theta \partial_\theta \zeta \right) + D_\mathrm{r} \left(\frac{1}{\sin^2\theta} \partial_\phi \psi \partial_\phi \zeta + \partial_\theta \psi \partial_\theta \zeta \right) \right\} \sin\theta \, \mathrm{d}\phi \, \mathrm{d}\theta \\
&= \int_0^\pi \int_0^{2\pi} \left\{ \sin\theta \partial_t \psi + \partial_\phi (b_\phi \psi) + \partial_\theta (\sin\theta b_\theta \psi) - D_\mathrm{r} \left(\partial_\phi \left(\frac{1}{\sin\theta} \partial_\phi \psi \right) + \partial_\theta (\sin\theta \partial_\theta \psi) \right) \right\} \zeta \, \mathrm{d}\phi \, \mathrm{d}\theta.
\end{aligned}$$

Hence, we obtain

$$\sin\theta \partial_t \psi + \partial_\phi (b_\phi \psi) + \partial_\theta (\sin\theta b_\theta \psi) - D_\mathrm{r} \left(\partial_\phi \left(\frac{1}{\sin\theta} \partial_\phi \psi \right) + \partial_\theta (\sin\theta \partial_\theta \psi) \right) = 0.$$

3.2. The fractional step method

For the numerical approximation of (11) on the unit sphere S^2 we use a longitude–latitude grid. For simplicity, we assume an equally spaced computational grid in the ϕ and the θ-direction with $\Delta\phi = \phi_{i+\frac{1}{2}} - \phi_{i-\frac{1}{2}}$, $i = 1, \ldots, M$ and $\Delta\theta = \theta_{j+\frac{1}{2}} - \theta_{j-\frac{1}{2}}$, $j = 1, \ldots, N$. Let the externally imposed velocity gradient be denoted by $\nabla_{\vec{x}} \vec{u}_{\text{ext}} = (u_{ij})_{i,j=1,2,3}$. We can now rewrite (11) into the conservative form

$$\kappa(\phi,\theta)\partial_t\psi(t,\phi,\theta) + \partial_\phi(a(\phi,\theta)\psi(t,\phi,\theta)) + \partial_\theta(b(\phi,\theta)\psi(t,\phi,\theta)) = (\mathscr{L}\psi)(t,\phi,\theta) \tag{15}$$

with

$$\kappa(\phi,\theta) := \sin\theta, \tag{16}$$

$$\mathscr{L}\psi := D_r\left(\partial_\phi\left(\frac{1}{\sin\theta}\partial_\phi\psi\right) + \partial_\theta(\sin\theta\partial_\theta\psi)\right), \tag{17}$$

$$\begin{aligned} a(\phi,\theta) &:= -u_{11}\sin\phi\cos\phi\sin\theta - u_{12}\sin^2\phi\sin\theta + u_{13}\cos\theta\sin\phi \\ &\quad + u_{21}\cos^2\phi\sin\theta + u_{22}\sin\phi\cos\phi\sin\theta - u_{23}\cos\theta\cos\phi, \\ b(\phi,\theta) &:= u_{11}\cos^2\phi\sin^2\theta\cos\theta + u_{12}\sin\phi\cos\phi\sin^2\theta\cos\theta - u_{13}\cos^2\theta\cos\phi\sin\theta \\ &\quad + u_{21}\cos\phi\sin^2\theta\sin\phi\cos\theta + u_{22}\sin^2\phi\sin^2\theta\cos\theta - u_{23}\sin\phi\cos^2\theta\sin\theta \\ &\quad + u_{31}\sin^3\theta\cos\phi + u_{32}\sin\phi\sin^3\theta - u_{33}\cos\theta\sin^2\theta. \end{aligned} \tag{18}$$

To obtain an approximation of (15), we use an operator splitting method, in which we alternate between solving the pure transport problem

$$\kappa(\phi,\theta)\partial_t\psi + \partial_\phi(a(\phi,\theta)\psi) + \partial_\theta(b(\phi,\theta)\psi) = 0 \tag{19}$$

and the heat equation

$$\kappa(\phi,\theta)\partial_t\psi = \mathscr{L}\psi. \tag{20}$$

Subproblem (19) will be solved by a high-resolution finite volume method and subproblem (20) will be solved by a second-order accurate finite difference method.

A second-order accurate operator splitting method is the Strang-splitting [29] which has the form

$$\Psi^{n+1} = L_{\text{heat}}^{\Delta t/2} L_{\text{trans}}^{\Delta t} L_{\text{heat}}^{\Delta t/2}\Psi^n, \tag{21}$$

i.e. the numerical solution of the Smoluchowski equation at time t^{n+1} is calculated from the numerical solution at time t^n by first applying the solution operator for the heat equation on the sphere over a half time step, followed by one time step of the finite volume method for advective transport, and another half time step of the heat equation solver. By using accurate methods for both subproblems, we will obtain a method for the full problem that is accurate for a large range of parameter values, in particular the large Deborah number regime.

3.3. A finite volume method for advective transport

On the one-dimensional unit sphere the Smoluchowski equation in the dilute regime with externally given velocity gradient $\nabla_{\vec{x}}\vec{u}_{\text{ext}} = (u_{ij})_{i,j=1,2}$ takes the form

$$\partial_t\psi + \partial_\phi(\psi(-u_{11}\sin\phi\cos\phi - u_{12}\sin^2\phi + u_{21}\cos^2\phi + u_{22}\sin\phi\cos\phi)) = D_r\partial_\phi^2\psi \tag{22}$$

with $\Psi := \Psi(t,\phi)$ and $\phi \in [0,2\pi)$. We thus want to construct a finite volume method for a scalar transport equation of the form

$$\partial_t\psi(t,\phi) + \partial_\phi(a(\phi)\psi(t,\phi)) = 0 \tag{23}$$

with a given function $a : [0,2\pi] \to \mathbb{R}$ and given initial values for ψ.

The construction of finite volume methods for conservation laws with spatially varying flux functions was studied in Bale et al. [2]. There a suitable decomposition of the flux differences at cell interfaces, the so-called *f*-wave approach, was introduced. However, in [2] it was assumed that the spatially varying velocity field does not change sign. For our application this assumption is not satisfied and we will therefore develop an *f*-wave approach that can be used in the more general situation.

A finite volume method for (23) has the general form

$$\Psi_i^{n+1} = \Psi_i^n - \frac{\Delta t}{\Delta\phi}\left(F_{i+\frac{1}{2}} - F_{i-\frac{1}{2}}\right), \tag{24}$$

where Ψ_i^n is an approximation to the cell average of the conserved quantity ψ in grid cell i (i.e. $[\phi_{i-\frac{1}{2}}, \phi_{i+\frac{1}{2}}]$) at time t^n and the F-terms are numerical fluxes calculated at grid cell interfaces. The numerical fluxes are Godunov fluxes calculated by solving generalized Riemann problems as described below. Second-order correction terms are included and limiters may be used to avoid non-physical oscillations near steep gradients in the solution profile. Using the f-wave approach, we can write the finite volume method in the form

$$\Psi_i^{n+1} = \Psi_i^n - \frac{\Delta t}{\Delta \phi}\left(\mathscr{Z}^2_{i-\frac{1}{2}} + \mathscr{Z}^1_{i+\frac{1}{2}}\right) - \frac{\Delta t}{\Delta \phi}\left(\tilde{F}_{i+\frac{1}{2}} - \tilde{F}_{i-\frac{1}{2}}\right), \tag{25}$$

where $\mathscr{Z}^{1,2}$ are first-order fluctuations and the $\tilde{F}$ terms are high-resolution correction terms.

We use a cell centered discretization of the spatially varying advection speed $a(\phi)$. Alternatively one could use an edge centered discretization of the advection speed, see [16]. For our discretization the *generalized Riemann problem* at the cell interface $\phi_{i-\frac{1}{2}}$ consists of the equation

$$\partial_t \psi + \partial_\phi\left(a_{i-\frac{1}{2}}(\phi)\psi\right) = 0 \quad \text{with } a_{i-\frac{1}{2}}(\phi) := \begin{cases} a_{i-1} := a(\phi_{i-1}) : \phi < \phi_{i-\frac{1}{2}}, \\ a_i := a(\phi_i) : \phi > \phi_{i-\frac{1}{2}} \end{cases} \tag{26}$$

together with the initial values

$$\psi(x, t^n) = \begin{cases} \Psi^n_{i-1} : \phi < \phi_{i-\frac{1}{2}}, \\ \Psi^n_i : \phi > \phi_{i-\frac{1}{2}}. \end{cases} \tag{27}$$

The structure of the solution of the Riemann problem is depicted in Fig. 1. If $a(\phi)$ does not change sign, then the conserved quantity ψ may be discontinuous across the cell interface $\phi_{i-\frac{1}{2}}$, see Fig. 1(a) and (b). Furthermore, there is a discontinuity moving to the right (with speed a_i) or to the left (with speed a_{i-1}) depending on the sign of $a(\phi)$. Since the flux is continuous across the interface, the middle state Ψ^* can be calculated by

$$\Psi^* = \begin{cases} a_{i-1}\Psi_{i-1}/a_i : a_{i-1}, a_i > 0, \\ a_i\Psi_i/a_{i-1} : a_{i-1}, a_i < 0. \end{cases}$$

If $a_{i-1} < 0$ and $a_i > 0$ (Fig. 1(c)) then the conserved quantity is moving away from the grid cell interface $\phi_{i-\frac{1}{2}}$ on both sides, leaving a vacuum in between, i.e. $\Psi^* = 0$. If $a_{i-1} > 0$ and $a_i < 0$, then a delta shock is forming right at the interface, see Fig. 1(d). Note that the structure of the Riemann problem (26) and (27) has similarities to the structure of the Riemann problem for the pressureless gas equations, see [17]. Also there vacuum states and delta shocks may arise.

The f-waves $\mathscr{Z}^{1,2}$ can now be calculated by performing a decomposition of the flux difference $a_i\Psi_i - a_{i-1}\ \Psi_{i-1}$. Note that the standard wave propagation algorithm (described in [15,16]) would instead

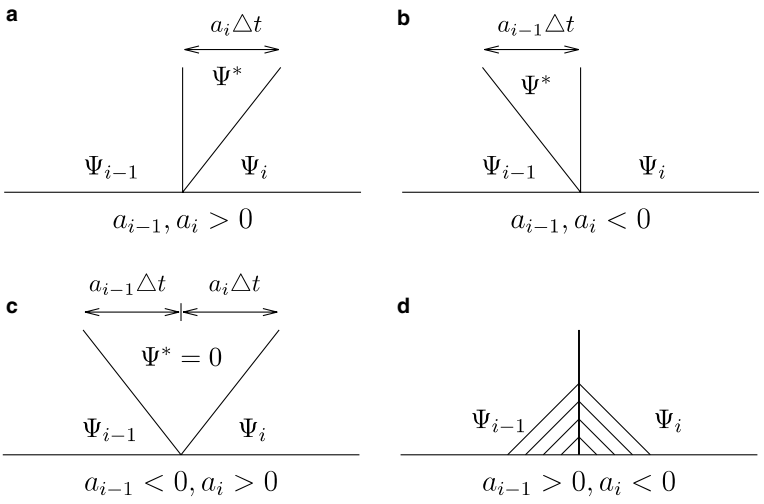

Fig. 1. Structure of the Riemann problem (26) and (27).

use a decomposition of the difference $\Psi_i - \Psi_{i-1}$ of the conserved quantity. The advantage of the f-wave method for conservation laws with spatially varying flux function lies in the fact that the flux is continuous across the cell interface although the conserved quantity may have a jump there. If $a(\phi)$ does not change sign (see [2]) then the entire flux difference can be carried by just one f-wave, i.e.

$$\mathscr{Z}_{i-\frac{1}{2}} = a_i\Psi_i - a_{i-1}\Psi_{i-1}$$

with no flux difference remaining at the cell interface. This means in particular that we do not have to calculate the quantity Ψ^*. Although this is trivial in the simple case considered here, it carries over to more difficult Riemann problems.

In order to extend the f-wave approach to the situation where the spatially varying advection speed may change sign, we decompose the flux difference at each cell interface into two f-waves, i.e.

$$a_i\Psi_i - a_{i-1}\Psi_{i-1} = \mathscr{Z}^1_{i-\frac{1}{2}} + \mathscr{Z}^2_{i-\frac{1}{2}}. \tag{28}$$

The first f-wave $\mathscr{Z}^1_{i-\frac{1}{2}}$ is used to update the conserved quantity in the grid cell to the left side of the cell interface while the second f-wave $\mathscr{Z}^2_{i-\frac{1}{2}}$ is used to update the conserved quantity in the grid cell at the right-hand side. We now obtain the algorithm:

If $a_{i-1}a_i > 0$, set $a_{i-\frac{1}{2}} := (a_{i-1} + a_i)/2$:

$$\begin{aligned}
\text{if } a_{i-\frac{1}{2}} < 0: \quad & \mathscr{Z}^1_{i-\frac{1}{2}} := a_i\Psi_i - a_{i-1}\Psi_{i-1}, \qquad s^1_{i-\frac{1}{2}} := a_{i-\frac{1}{2}},\\
& \mathscr{Z}^2_{i-\frac{1}{2}} := 0, \qquad s^2_{i-\frac{1}{2}} := 0,\\
\text{if } a_{i-\frac{1}{2}} > 0: \quad & \mathscr{Z}^1_{i-\frac{1}{2}} := 0, \qquad s^1_{i-\frac{1}{2}} := 0,\\
& \mathscr{Z}^2_{i-\frac{1}{2}} := a_i\Psi_i - a_{i-1}\Psi_{i-1}, \qquad s^2_{i-\frac{1}{2}} := a_{i-\frac{1}{2}}.
\end{aligned}$$

If $a_{i-1} < 0 < a_i$, i.e. vacuum:

$$\begin{aligned}
&\mathscr{Z}^1_{i-\frac{1}{2}} := -a_{i-1}\Psi_{i-1}, \quad s^1_{i-\frac{1}{2}} := a_{i-1}/2,\\
&\mathscr{Z}^2_{i-\frac{1}{2}} := a_i\Psi_i, \quad s^2_{i-\frac{1}{2}} := a_i/2.
\end{aligned}$$

If $a_{i-1} > 0$ and $a_i < 0$, i.e. delta shock:

$$\begin{aligned}
&\mathscr{Z}^1_{i-\frac{1}{2}} := (a_i\Psi_i - a_{i-1}\Psi_{i-1})/2, \quad s^1_{i-\frac{1}{2}} := 0,\\
&\mathscr{Z}^2_{i-\frac{1}{2}} := (a_i\Psi_i - a_{i-1}\Psi_{i-1})/2, \quad s^2_{i-\frac{1}{2}} := 0.
\end{aligned}$$

The finite volume method using these f-waves can be written in the form (25) with the second-order correction terms

$$\tilde{F}_{i-\frac{1}{2}} = \frac{1}{2}\sum_{p=1}^{2} \operatorname{sgn}\left(s^p_{i-\frac{1}{2}}\right)\left(1 - \frac{\Delta t}{\Delta\phi}|s^p_{i-\frac{1}{2}}|\right)\mathscr{Z}^p_{i-\frac{1}{2}}. \tag{29}$$

In the second-order correction terms, we also need wave speeds $s^{1,2}_{i-\frac{1}{2}}$ associated to the f-waves $\mathscr{Z}^{1,2}_{i-\frac{1}{2}}$. If $a(\phi)$ does not change sign, several choices of the wave speed $s_{i-\frac{1}{2}}$ lead to a second-order accurate f-wave method, assuming that the functions a and ψ are sufficiently smooth, see [2]. In this case, $s_{i-\frac{1}{2}}$ is an eigenvalue of an approximative Jacobian matrix of the flux $a(\phi)q(t,\phi)$ at the interface $\phi_{i-\frac{1}{2}}$. In order to construct a second-order accurate f-wave method, we need to approximate the Jacobian matrix with order $\mathcal{O}(\Delta\phi)$. Furthermore, the approximation of the Jacobian matrix must be consistent at all grid cell interfaces. Here, we have approximated the Jacobian matrix by $A_{i-\frac{1}{2}} = (a_{i-1} + a_i)/2$, i.e. both for $a(\phi) > 0$ and $a(\phi) < 0$ the approximation of the Jacobian matrix is equivalent. Second-order accuracy can be shown by Taylor series expansion.

On the sphere we approximate a transport equation of the form (19) with capacity function and spatially varying flux functions. The finite volume method has the general form

$$\Psi^{n+1}_{i,j} = \Psi^n_{i,j} - \frac{\Delta t}{\kappa_{i,j}\Delta\phi}\left(F_{i+\frac{1}{2},j} - F_{i-\frac{1}{2},j}\right) - \frac{\Delta t}{\kappa_{i,j}\Delta\theta}\left(G_{i,j+\frac{1}{2}} - G_{i,j-\frac{1}{2}}\right), \tag{30}$$

where $\Psi^n_{i,j}$ is an approximation to the cell average of the quantity ψ in grid cell (i,j) at time t^n, and $\kappa_{i,j}$ is the cell centered value of the capacity function. Furthermore, $F_{i+\frac{1}{2},j}$ and $G_{i,j+\frac{1}{2}}$ are numerical fluxes calculated at the grid cell interfaces $(\phi_{i+\frac{1}{2}}, \theta_j)$ and $(\phi_i, \theta_{j+\frac{1}{2}})$, respectively. Periodic boundary conditions are used at the boundaries of the computational grid in the ϕ-direction.

The numerical method is a variant of the high-resolution wave propagation algorithm of LeVeque [15,16]. This is a truly multi-dimensional method in the sense that it does not use dimension splitting. The numerical fluxes are Godunov fluxes that result from solving one-dimensional Riemann problems both in the ϕ-direction as well as in the θ-direction using the f-wave approach described above. Second-order correction terms are included in analogy to the one-dimensional case. In addition the algorithm also calculates a transverse wave propagation as part of the second-order correction terms.

The stability condition is the usual CFL condition which in the presence of the capacity function reads

$$\Delta t \max_{i,j} \left(\frac{|a_{i,j}|}{\kappa_{i,j}\Delta\phi}, \frac{|b_{i,j}|}{\kappa_{i,j}\Delta\theta} \right) \leqslant 1. \tag{31}$$

Near the north and the south pole the capacity function $\kappa(\phi,\theta) = \sin\theta$ becomes very small, leading to the so-called *pole singularity*. Note however that in our application this does not cause a stability problem at least as long as we restrict our considerations to a two-dimensional macroscopic velocity field. In this case, all non-zero terms arising in formula (18) contain $\sin\theta$ and therefore the division by κ in the finite volume method does not lead to a strong restriction of the time step.

Nevertheless, the use of a Cartesian computational grid requires a small modification of the finite volume method at the north and the south pole, where the grid cells on the sphere degenerate to triangles. Here, we model the grid cells at the poles (i.e. the grid cells in the first and the last row of the computational mesh) as two single grid cells.

Recently, Rossmanith [28] developed a wave propagation method for hyperbolic problems on the sphere using a cubed sphere grid, which covers the sphere with six identical grid patches. With such a grid the pole singularity is avoided. Numerical boundary conditions have to be implemented in order to model wave propagation between different grids. The diffusion terms arising in our application would further complicate the method, this has not been implemented so far. Another alternative would be to use an unstructured grid on the sphere based on triangles for example.

3.4. Finite difference methods for the heat equation on the sphere

For the approximation of the heat equation on the sphere $\partial_t \Psi = D_r \nabla^2_{\vec{n}} \Psi$ a finite difference method is used. We make use of routines from Fishpack [1] which provide a solver for the Helmholz equation on the sphere, i.e. for $\lambda\Psi + \nabla^2_{\vec{n}}\Psi = F$ (with given F and $\lambda < 0$). The grid points used by a staggered finite difference grid on the sphere in computational space agree with the cell average values used by the finite volume method described in the previous section. In order to obtain a solver for the heat equation, we need to incorporate an implicit ODE solver. In the context of operator-splitting methods, it is essential to use a multistage *one-step* method, since the use of Ψ from previous time steps would not be suitable. Here, we used the TR-BDF2 method (introduced in [3]) which is second-order accurate and L-stable. One time step (from t^n to t^{n+1}) takes the form

$$\begin{aligned} \Psi^*_{i,j} &= \Psi^n_{i,j} + \frac{\Delta t}{4}\left(\nabla^2_{\vec{n}}\Psi^n_{i,j} + \nabla^2_{\vec{n}}\Psi^*_{i,j}\right), \\ \Psi^{n+1}_{i,j} &= \frac{1}{3}\left(4\Psi^*_{i,j} - \Psi^n_{i,j} + \Delta t \nabla^2_{\vec{n}}\Psi^{n+1}_{i,j}\right). \end{aligned} \tag{32}$$

The Laplace operator is discretized by the standard 5-point stencil.

3.5. Numerical results for the Smoluchowski equation in the dilute regime

In this section, we will illustrate the performance of our numerical method for the Smoluchowski equation in the dilute regime for *elongational flow*. In this case, we can compare our numerical solution with the exact solution.

Example 3.1. We calculate steady-state solutions of the Smoluchowski equation in the dilute regime, i.e. Eq. (15) with (16)–(18). The initial values on the sphere are set to $\psi(0,\phi,\theta) = 1/4\pi$. The externally imposed velocity gradient has the form

$$\nabla_{\vec{x}}\vec{u}_{\text{ext}} = \ell \begin{pmatrix} 2 & 0 & 0 \\ 0 & -1 & 0 \\ 0 & 0 & -1 \end{pmatrix}$$

with $\ell = \pm 1$. For $\ell > 0$, we obtain uniaxial extensional motion, i.e. a full alignment of the director in one direction. For $\ell < 0$ we observe biaxial extensional motion, i.e. the axes align strongly in a plane, but within that plane show no further tendency to align. The rotational diffusion constant is set to $D_r = 1/10$. Note that the Deborah number in this test case is $De = 20$.

Fig. 2 shows plots of the numerical solution and Table 1 shows the error both in the L_1-norm and the L_∞-norm for the case of uniaxial extensional motion calculated using the formulas

$$\|\text{error}\|_{L_1} = \sum_{i=1}^{M}\sum_{j=1}^{N} |\Psi_{i,j}^{\text{exact}} - \Psi_{ij}| \sin\theta_j \Delta\phi\Delta\theta, \tag{33}$$

$$\|\text{error}\|_{\infty} = \max_{i,j} |\Psi_{i,j}^{\text{exact}} - \Psi_{i,j}|, \tag{34}$$

where $\Psi_{i,j}$ is a numerical solution that has converged to the steady state and $\Psi_{i,j}^{\text{exact}}$ is the exact steady-state solution in grid cell (i,j). We also show the experimental order of convergence (EOC) obtained by comparing the error on two different grids.

The exact steady-state solution for uniaxial extensional motion has the form

$$\psi^{\text{exact}}(\phi,\theta) = C \exp\left(-\frac{3}{2D_r}(1-\cos^2(\phi)\sin^2(\theta))\right),$$

where C is a constant that can be obtained by the condition (1). For $D_r = 1/10$ we obtain $C = 2.30122$.

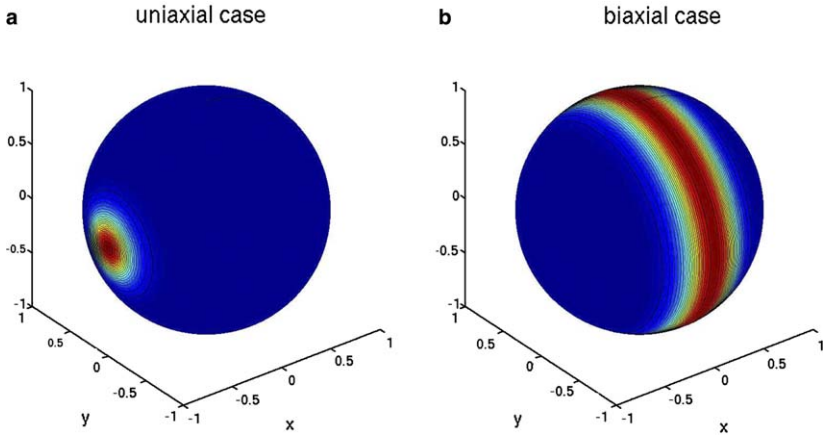

Fig. 2. Numerical solution of the Smoluchowski equation for (a) uniaxial (i.e. $\ell = 1$) and (b) biaxial (i.e. $\ell = -1$) extensional motion with $D_r = 1/10$.

Table 1
Accuracy study for uniaxial extensional motion

M/N	L_1-error	EOC	L_∞-error	EOC
40/20	0.06001424		0.10916803	
80/40	0.01497276	2.03	0.04779091	1.19
160/80	0.00365058	2.03	0.01558344	1.62
320/160	0.00090492	2.01	0.00439733	1.82
640/320	0.00022760	1.99	0.00119370	1.88

The solution of the Smoluchowski equation in the dilute regime with externally given velocity field corresponding to shear flow will be described in Section 4, where we consider the coupled micro–macro problem.

Note that our numerical method for the microscopic solution structure can also be used in the semi-dilute case if the diffusion is modeled by Eq. (7). The only difference compared to the dilute regime is that the diffusion constant has to be updated during each time step of the numerical method.

3.6. The solution of the Smoluchowski equation in the concentrated regime

In the concentrated regime, the microscopic solution structure of rod orientation shows a complex behavior which depends on the shear velocity and the parameter U. This was studied by Fafaoni et al. [5] for an externally given shear flow using tools of bifurcation analysis. See also earlier work by Larson and Öttinger [11]. For small values of U, a unique steady-state microscopic solution exists. For U large enough different microscopic solution structures can be observed depending on the strength of the shear velocity. At high shear rates the orientational distribution function converges to a steady state, the so-called *flow-aligning regime*. At low or intermediate shear rates three different kinds of time periodic solutions have been found: The *tumbling regime* is observed at low shear rates when the initial orientation of the director lies in the shear plane. This regime is characterized by a rotation of the director within the shear plane. (The angular velocity is highly non-uniform: the director flips from a flow-aligned position to the next.) The *wagging regime*, i.e. a partial rotation of the director in the shear plane, is observed at intermediate shear rates. For out-of-plane initial conditions the director may reach a *kayaking* orbit, i.e. the director rotates out of the shear plane but not orthogonal. Furthermore, for out-of-plane initial conditions and low shear rates the stationary *log rolling regime*, with the director oriented along the vorticity axis, can be observed. It is unlikely that such a rich microscopic behavior can be modeled by a single macroscopic model.

In the concentrated regime, we can use a numerical method very similar to those described above. The only difference is that the formulas for the spatially varying velocity field, i.e. a and b in Eq. (15), have to be extended and now also depend on $\psi(t,\phi,\theta)$. This means that the velocity field has to be updated during each time step. We rewrite the Smoluchowski equation for the concentrated regime (8) into the form

$$\kappa(\phi,\theta)\partial_t\psi + \partial_\phi(\tilde{a}(t,\phi,\theta)\psi) + \partial_\theta(\tilde{b}(t,\phi,\theta)\psi) = g(\psi) \tag{35}$$

with κ and g as in (16) and (17), respectively. Note that

$$\nabla_{\vec{n}}\cdot(\psi\nabla_{\vec{n}}V_{\mathrm{ev}}) = \frac{1}{\sin\theta}\left(\frac{1}{\sin\theta}\partial_\phi(\psi(t,\phi,\theta)\partial_\phi V_{\mathrm{ev}}) + \partial_\theta(\sin\theta\psi(t,\phi,\theta)\partial_\phi V_{\mathrm{ev}})\right). \tag{36}$$

We can thus write Eq. (8) in the form (35) using a velocity field of the form

$$\begin{aligned}\tilde{a}(t,\phi,\theta) &:= a(\phi,\theta) - D_{\mathrm{r}}\frac{1}{\sin\theta}\psi(t,\phi,\theta)\partial_\phi V_{\mathrm{ev}}(t,\phi,\theta),\\ \tilde{b}(t,\phi,\theta) &:= b(\phi,\theta) - D_{\mathrm{r}}\sin\theta\psi(t,\phi,\theta)\partial_\theta V_{\mathrm{ev}}(t,\phi,\theta).\end{aligned} \tag{37}$$

Here

$$V_{\mathrm{ev}}(t,\phi,\theta) := U\int_0^\pi\int_0^{2\pi}\psi(t,\phi',\theta')\sin\theta'(1-(\sin\theta\sin\theta'\cos(\phi-\phi')+\cos\theta\cos\theta')^2)\,\mathrm{d}\phi'\,\mathrm{d}\theta' \tag{38}$$

and $a(\phi,\theta)$, $b(\phi,\theta)$ are given in Eq. (18). In order to calculate the numerical solution at time t^{n+1}, we use a spatially varying velocity field $\tilde{a},\tilde{b}$ where the term modeling the excluded volume effect is evaluated using Ψ from the previously calculated time steps. To obtain (at time t^{n+1}) a second-order accurate approximation of a transport equation with time-dependent spatially varying velocity field using the method described in Section 3, we need discrete values of the velocity field at the intermediate time $t^{n+\frac{1}{2}}$, i.e. we need to use $\tilde{a}(t^{n+\frac{1}{2}},\phi,\theta)$, $\tilde{b}(t^{n+\frac{1}{2}},\phi,\theta)$. Here those values were calculated by extrapolation using the numerical solution Ψ^n and Ψ^{n-1} from previous time steps:

$$\begin{aligned}\tilde{a}(t^{n+\frac{1}{2}},\phi,\theta) &:= \left(1+\frac{t^{n+1}-t^n}{2(t^n-t^{n-1})}\right)\tilde{a}(t^n,\phi,\theta)-\frac{t^{n+1}-t^n}{2(t^n-t^{n-1})}\tilde{a}(t^{n-1},\phi,\theta),\\ \tilde{b}(t^{n+\frac{1}{2}},\phi,\theta) &:= \left(1+\frac{t^{n+1}-t^n}{2(t^n-t^{n-1})}\right)\tilde{b}(t^n,\phi,\theta)-\frac{t^{n+1}-t^n}{2(t^n-t^{n-1})}\tilde{b}(t^{n-1},\phi,\theta).\end{aligned} \tag{39}$$

Our numerical method is able to reproduce all the solution structures mentioned above. Here, we only show numerical results for the wagging regime.

Example 3.2. We approximate the Smoluchowski equation in the concentrated regime, i.e. Eq. (35) with (16), (17) and (37). The externally imposed velocity gradient has the form

$$\nabla_{\vec{x}}\vec{u}_{\text{ext}} = \begin{pmatrix}0 & 1 & 0\\ 0 & 0 & 0\\ 0 & 0 & 0\end{pmatrix}.$$

Furthermore we use $D_r = 1/10$ and $U = 10$. The initial values are set to $\psi(0,\phi,\theta) = 1/4\pi$, i.e. uniform distribution of director orientations.

Numerical results at different times are shown in Fig. 3. Results of a numerical accuracy study are shown in Table 2. Since we do not know the exact solution for this test case, we have compared our numerical solution on different grids with a highly resolved numerical solution that was calculated on a grid with 1800×900 grid cells. Results of the convergence test, which confirm second-order convergence rates, are shown for time $t = 4$ and $t = 14$ (corresponding to the first and the fifth plot in Fig. 3).

A coupled micro–macro problem for shear flow in the concentrated regime will be considered in Section 5.

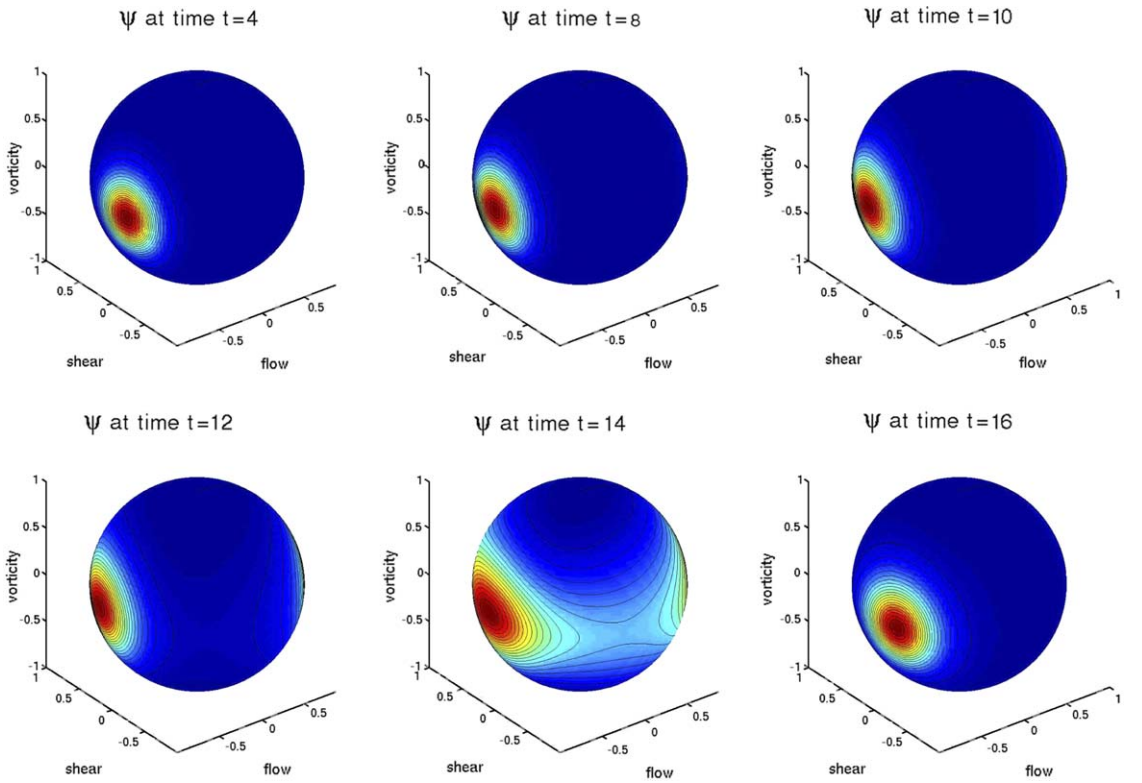

Fig. 3. Numerical approximation of the Smoluchowski equation in the concentrated regime showing time periodic wagging. grid: $M = 160$, $N = 80$.

Table 2
Accuracy study for Smoluchowski equation in the concentrated regime

M/N	$t=4$		$t=14$	
	L_1-error	EOC	L_1-error	EOC
40/20	0.03397236		0.03503204	
120/60	0.00361421	2.04	0.00275919	2.31
360/180	0.00037575	2.06	0.00027765	2.09

4. The shear flow problem and the spurt phenomenon in the dilute regime

Let $\vec{u} = (u(x,y,z), v(x,y,z), w(x,y,z))^{\mathrm{t}}$, $\vec{x} = (x,y,z)^{\mathrm{t}}$, $\vec{F}_{\mathrm{ext}} = (F^x_{\mathrm{ext}}, F^y_{\mathrm{ext}}, F^z_{\mathrm{ext}})^{\mathrm{t}}$ and $\sigma = (\sigma_{i,j})_{i,j=1,\ldots,3}$. We now consider the simplest possible coupled flow problem for suspensions of rod-like molecules, i.e. shear flow with macroscopic velocity that takes the form $\vec{u} = (u(y),0,0)^{\mathrm{T}}$. In this case, the micro–macro flow problem with no-slip boundary condition written in (ϕ,θ)-coordinates reads:

Microscopic Smoluchowski-equation:

$$\begin{aligned}&\partial_t(\sin\theta\psi) + \partial_\theta(u_y \sin\phi\cos\phi\sin^2\theta\cos\theta\psi) + \partial_\phi(-u_y\sin\theta\sin^2\phi\psi)\\ &\quad = D_{\mathrm{r}}\left(\partial_\theta(\sin\theta\psi_\theta) + \partial_\phi\left(\frac{1}{\sin\theta}\psi_\phi\right)\right).\end{aligned} \tag{40}$$

Macroscopic flow equation with boundary condition:

$$\begin{aligned}&\partial_{yy}u + \partial_y\sigma_{2,1} = -F^x_{\mathrm{ext}} \quad \text{on the interval } \left[-\frac{1}{2},\frac{1}{2}\right],\\ &u(-1/2) = u(1/2) = 0.\end{aligned} \tag{41}$$

Elastic stress:

$$\sigma_{2,1} = 3\int_0^\pi\int_0^{2\pi}\psi\sin^3\theta\cos\phi\sin\phi\,\mathrm{d}\phi\,\mathrm{d}\theta. \tag{42}$$

Given a constant externally imposed velocity gradient $\nabla_x\vec{u}_{\mathrm{ext}}$ the Smoluchowski equation (40) has a unique stationary solution $\psi(\vec{n})$. Via (42), this defines a mapping from deformation rate to elastic stress

$$\begin{aligned}&\nabla_x\vec{u}_{\mathrm{ext}} \mapsto \sigma,\\ &\nabla_{\vec{n}}\cdot(P_{\vec{n}^\perp}\nabla_{\vec{x}}\vec{u}_{\mathrm{ext}}\vec{n}\psi(\vec{n})) = D_{\mathrm{r}}\nabla^2_{\vec{n}}\psi(\vec{n}).\end{aligned} \tag{43}$$

After appropriate rescaling with D_{r} this mapping is universal. A key observation is that this map is non-monotone. Fig. 4(a) shows a numerical calculation of the non-monotone curve of the shear velocity versus the {1–2}-component of the elastic stress for $D_{\mathrm{r}} = 1$. As a consequence, the mapping

$$\begin{aligned}&\nabla_x\vec{u}_{\mathrm{ext}} \mapsto \frac{1}{2}(\nabla_x\vec{u}_{\mathrm{ext}} + \nabla^t_x\vec{u}_{\mathrm{ext}}) + \sigma,\\ &\nabla_{\vec{n}}\cdot(P_{\vec{n}^\perp}\nabla_{\vec{x}}\vec{u}_{\mathrm{ext}}\vec{n}\psi(\vec{n})) = D_{\mathrm{r}}\nabla^2_{\vec{n}}\psi(\vec{n}),\end{aligned} \tag{44}$$

which relates the deformation rate to the total stress is non-monotone for sufficiently small D_{r}. Fig. 4(b) shows a plot of (44) using $D_{\mathrm{r}} = 1/1000$. A consequence of this non-monotonicity is that there exist steady-state macroscopic solutions of the coupled problem with discontinuous shear velocity, see [24] for an analytical proof.

There are models with macroscopic constitutive equation, e.g. the JSO-model, that show in the highly elastic regime the same non-monotone behavior for shear velocity vs. total stress. We found that in the dilute regime the steady-state solution structure for shear flow, obtained by the micro–macro model, agrees with the steady-state solution structure predicted by the JSO-model. Before we present the

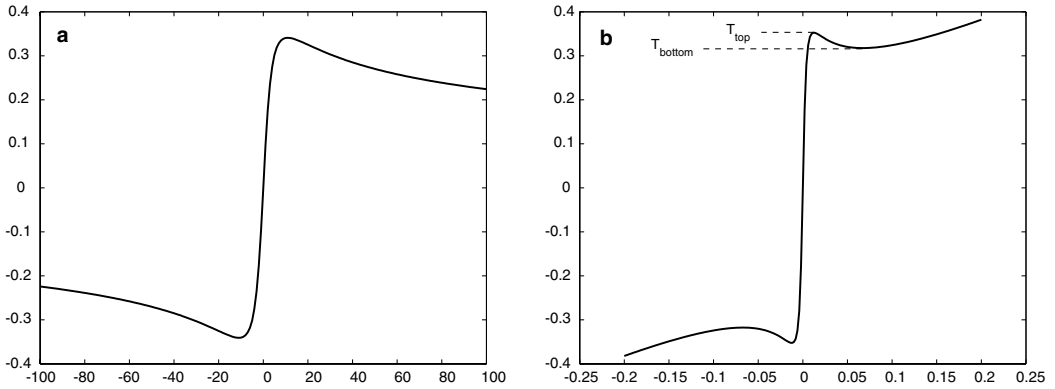

Fig. 4. (a) Non-monotonicity in shear velocity vs. elastic stress for $D_r = 1$. (b) The mapping shear velocity vs. total stress is non-monotone assuming D_r is small enough ($D_r = 1/1000$).

calculations for the micro–macro model we will summarize some known results for the JSO-model, see [18–20] for details.

4.1. Steady-state solutions of the shear flow problem for the JSO-model

In the shear flow situation considered in this section, steady-state solutions of the JSO-model satisfy the equations

$$\sigma = \frac{u_y}{1+u_y^2},$$
$$\sigma + \varepsilon u_y = -yF_{\text{ext}}, \quad y \in [-1/2, 0],$$

where u is the velocity, σ is the elastic stress component, $T := \sigma + \varepsilon u_y$ is the total stress and F_{ext} is an external forcing that is assumed to be constant.

The mapping from shear velocity to total stress $u_y \mapsto \varepsilon u_y + \sigma$ is non-monotone for $\varepsilon < 1/8$, see Fig. 5(a). It has been proposed by Malkus et al. [18–20] that this non-monotonicity may explain the spurt phenomenon. For a given total stress, there are two possible values for the shear rate once a critical value is reached (the decreasing part of the curve can be ignored for stability reasons). The sudden increase of the flow rate observed in the spurt regime was explained by the two shear rates coexisting in a flow, with the higher shear rate close to the wall. Malkus et al. analyze the velocity profile for one-dimensional shear flow through a slit

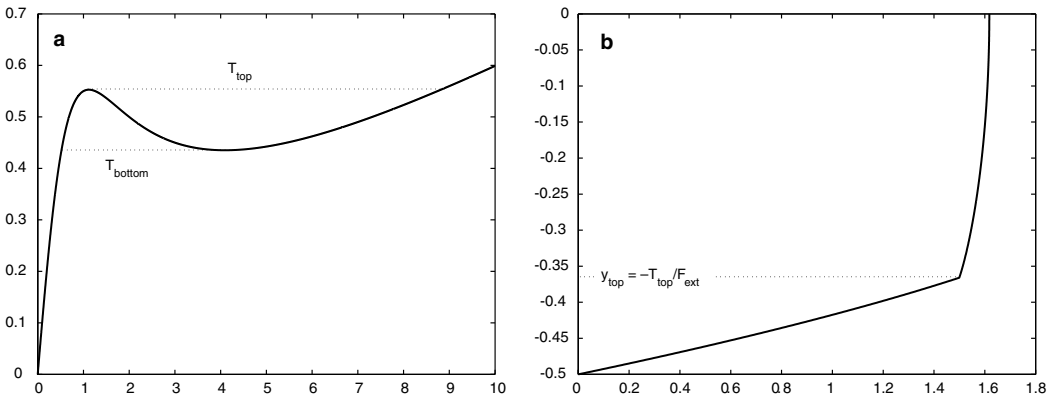

Fig. 5. (a) The mapping shear velocity vs. total stress for the JSO-model is non-monotone assuming ε is small enough, here $\varepsilon = 1/20$. (b) Top-jumping solution of JSO-model for $F_{\text{ext}} = 1.5$, $\varepsilon = 1/20$. Plot of u vs. y.

die in the spurt regime. They determine steady-state solutions for several different situations by analyzing systems of ordinary differential equations.

One experiment is the case of quasi static loading in which the volume forcing term F_{ext} is increased in small steps such that the steady state is reached at each step. Under loading a smooth (i.e., classical) velocity profile is observed as long as $|y_{\text{wall}}|F_{\text{ext}} \leqslant T_{\text{top}}$. (See Fig. 5(a) for the notation T_{top} and T_{bottom}. Furthermore y_{wall} denotes the position of the boundary, i.e. in our example $|y_{\text{wall}}| = 1/2$.) Past the point T_{top} the velocity profile develops a kink near the wall, as the fluid near the wall jumps to the higher shear rate, and the bulk of the fluid remains at lower shear rate. This jump in the shear rate at T_{top} is called *top-jumping*. As the volume forcing is increased further, the kink moves away from the boundary. The location of the kink for a top-jumping solution is $y_{\text{top}} = -T_{\text{top}}/F_{\text{ext}}$. Fig. 5(b) shows such a top-jumping velocity profile of the JSO-model with $F_{\text{ext}} = 1.5$ and $\varepsilon = 1/20$. The plot shows $u(y)$ vs. y.

Another experiment is unloading. Here we start with a top-jumping solution and decrease the forcing such that $T_{\text{bottom}} < |y_{\text{wall}}|F^x_{\text{ext}} < T_{\text{top}}$. For this experiment, a bottom-jumping macroscopic solution is observed, i.e. the jump in the velocity gradient is observed at the position $y_{\text{bottom}} = -T_{\text{bottom}}/F_{\text{ext}}$.

Our numerical calculations (shown in Section 4.2) suggest that the same behavior for the macroscopic velocity profile can be obtained for our multiscale model in the dilute regime. In the concentrated regime, we observe the formation of a microstructure in the macroscopic velocity profile (see Section 5). This cannot be obtained by the macroscopic JSO-model.

4.2. Numerical results for the coupled micro–macro model

We now perform numerical simulations for the coupled multiscale system (40)–(42) using $D_r = 1/1000$. In the first experiment, the forcing is increased up to a value $F^x_{\text{ext}} \leqslant 0.68$ which is slightly below the value $2 \cdot T_{\text{top}} \approx 0.70$ but larger than $2 \cdot T_{\text{bottom}} \approx 0.63$. The macroscopic velocity profile is shown in Fig. 6(a) where we plot $u(y)$ vs. y. In agreement with the above-mentioned analytical results for the JSO-model, we observe a classical solution. If we increase the forcing to the value $F^x_{\text{ext}} = 0.8$, the steady-state velocity profile changes dramatically and we observe a top-jumping macroscopic solution, see Fig. 6(b). In our third experiment, we start with a top-jumping macroscopic solution obtained with $F^x_{\text{ext}} = 3$. We decrease the forcing up to $F^x_{\text{ext}} = 0.8$, i.e. the same value as used in the previous experiment. For this unloading experiment, we observe a bottom-jumping steady-state solution, see Fig. 6(c).

In Fig. 7, we show the microscopic solution structure as it arises at a single point in the smooth flow region (see Fig. 7(a)) and inside the boundary layer (Fig. 7(c)). In the small Deborah number regime, the rod orientation is nearly uniformly distributed in the plane spanned by flow direction and shear direction with a light preference of rods oriented in a 45° angle to the flow direction. In the large Deborah number regime, i.e. inside

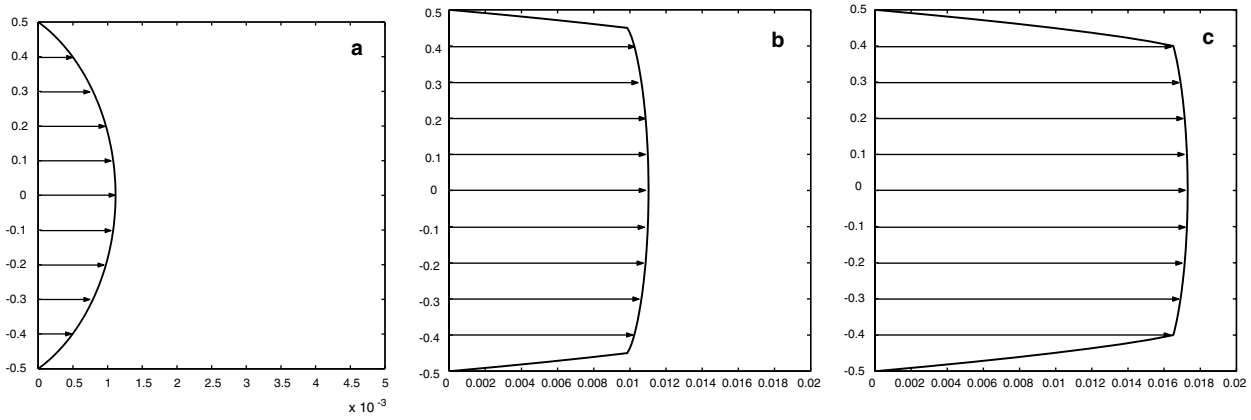

Fig. 6. Macroscopic velocity profiles observed for loading and unloading experiment: (a) classical solution ($F^x_{\text{ext}} = 0.68$), (b) top-jumping solution ($F^x_{\text{ext}} = 0.8$), (c) bottom-jumping solution ($F^x_{\text{ext}} = 0.8$). (Note the different scaling of the x-axis).

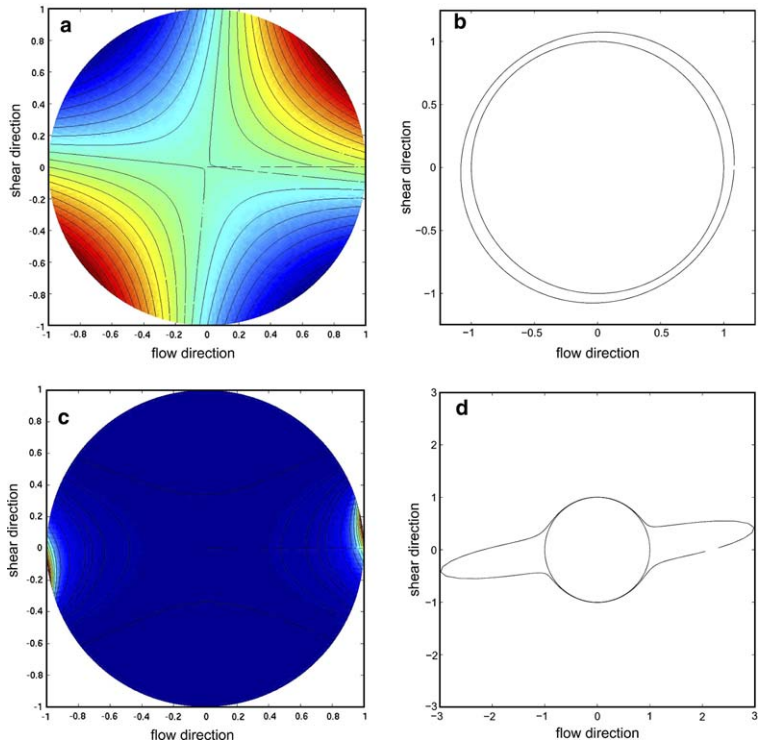

Fig. 7. Microscopic solution for probability distribution of rod orientations; (a,c) contour plots of Ψ for small and large Deborah number, respectively. (b,d) graph of Ψ in the plane of flow direction and shear direction for small and large Deborah number.

the boundary layer of a spurt solution, the rod orientation is nearly aligned with the flow direction. Figs. 7(b) and (d) show the graph of Ψ in the flow direction–shear direction plane. In (a) and (c), we show level sets of Ψ plotted on the sphere and viewed from the positive vorticity axis. In (b) and (d), we plot a graph of Ψ in the plane spanned by the flow and the shear direction.

5. Simulations of the coupled flow problem in the concentrated regime

We now consider coupled flow problems in the concentrated regime. As in the previous section, we assume that the macroscopic velocity field has the form $\vec{u} = (u(y), 0, 0)^{\mathrm{T}}$. In the concentrated regime excluded volume effects need to be included in the calculation of the microscopic equation for rod orientation (compare with Eq. (8)) and in the calculation of the macroscopic elastic stress (compare with Eq. (10)). Here, we describe different numerical experiments with macroscopic solutions that show the spurt phenomenon.

Depending on the strength of the parameter U in the Maier–Saupe potential, the macroscopic solutions in the concentrated regime show a more complex structure than in the dilute regime. For small values of U, the Smoluchowski equation (8) has for all shear rates a unique stationary solution. These solutions have the director always in the shear plane. (Note that this was also observed in [5].) For the steady-state solution, we can consider the mapping from deformation rate to elastic stress. As in the dilute regime, this mapping is non-monotone. Fig. 8 shows a numerical simulation of shear velocity vs. elastic stress for $D_r = 1$ and $U = 0$ (i.e. the dilute regime) as well as for $U = 1$, $U = 2$ and $U = 3$. We thus expect spurt macroscopic solutions for D_r small enough and a volume forcing term F^x_{ext} large enough.

Example 5.1. The coupled micro–macro shear flow problem in the concentrated regime is solved for $y \in [-\frac{1}{2}, \frac{1}{2}]$ with boundary conditions $u(-1/2) = u(1/2) = 0$. The rotational diffusion is set to $D_r = 1/1000$ and the volume forcing term is $F^x_{\mathrm{ext}} = 1$. The parameter U in the Maier–Saupe potential varies in our experiments

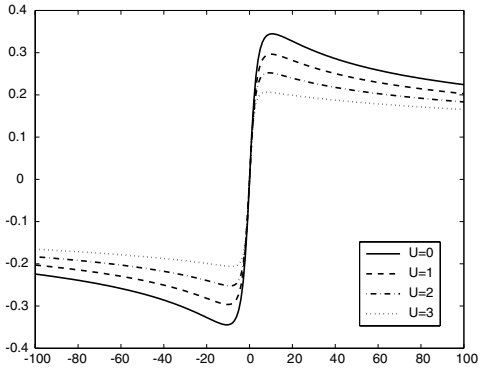

Fig. 8. Shear velocity vs. elastic stress for $D_r = 1$ and different values of the parameter U in the Maier–Saupe potential, i.e. $U = 0$, $U = 1$, $U = 2$ and $U = 3$.

and is set to $U = 1$ and $U = 20$. The microscopic initial values for rod orientation are set to be the uniform distribution.

In the case $U = 1$, the microscopic problem for rod orientation has for any shear rate a unique steady state. In analogy to the dilute case we can consider the curve of shear velocity vs. total stress which is non-monotone for D_r small enough, see Fig. 9(a). A numerical calculation of the macroscopic velocity is shown in Fig. 9(b). Note that we observe a top-jumping macroscopic solution.

For larger values of U, the Smoluchowski equation in the concentrated regime no longer has a unique stationary solution. Instead, at least for smaller shear velocities, time periodic tumbling and wagging solutions may be observed. Therefore, we expect that the macroscopic solution structure also depends on time. If the shear velocity is large enough the microscopic solution is a steady state flow aligned solution. Such microscopic solutions can be observed inside the boundary layer of the spurt solution in Fig. 10. For lower shear rates, which arise in the bulk of the macroscopic flow, the microscopic solution is a time periodic tumbling or wagging solution characterized by a full or partial rotation of the director in the plane spanned by flow direction and shear direction. The frequency of the rotational motion depends on the local shear rate. In our case of a Poiseuille-type velocity profile, the shear rate and thus the tumbling and the wagging frequency varies in the y-direction. This generates a spatial twist in the director orientation which increases over time. This is reflected in the increasing number of oscillations observed in the macroscopic velocity outside the boundary layer, see Fig. 10. An increase of the number of oscillations with time can also be observed in the plots of elastic stress vs. y, which are also shown in Fig. 10. In Fig. 11, we indicate the average orientation of the rods as it can be observed at different locations of the macroscopic flow domain at different times.

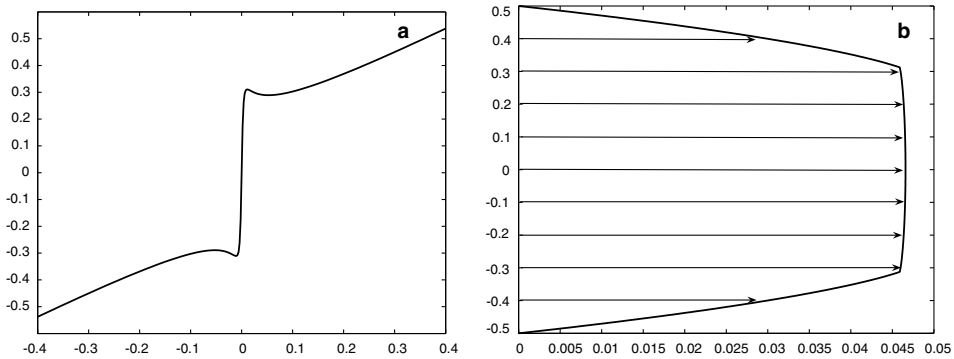

Fig. 9. (a) Shear velocity vs. total stress in the concentrated regime with $D_r = 1/1000$ and $U = 1$; (b) macroscopic velocity profile for Example 5.1 with $U = 1$.

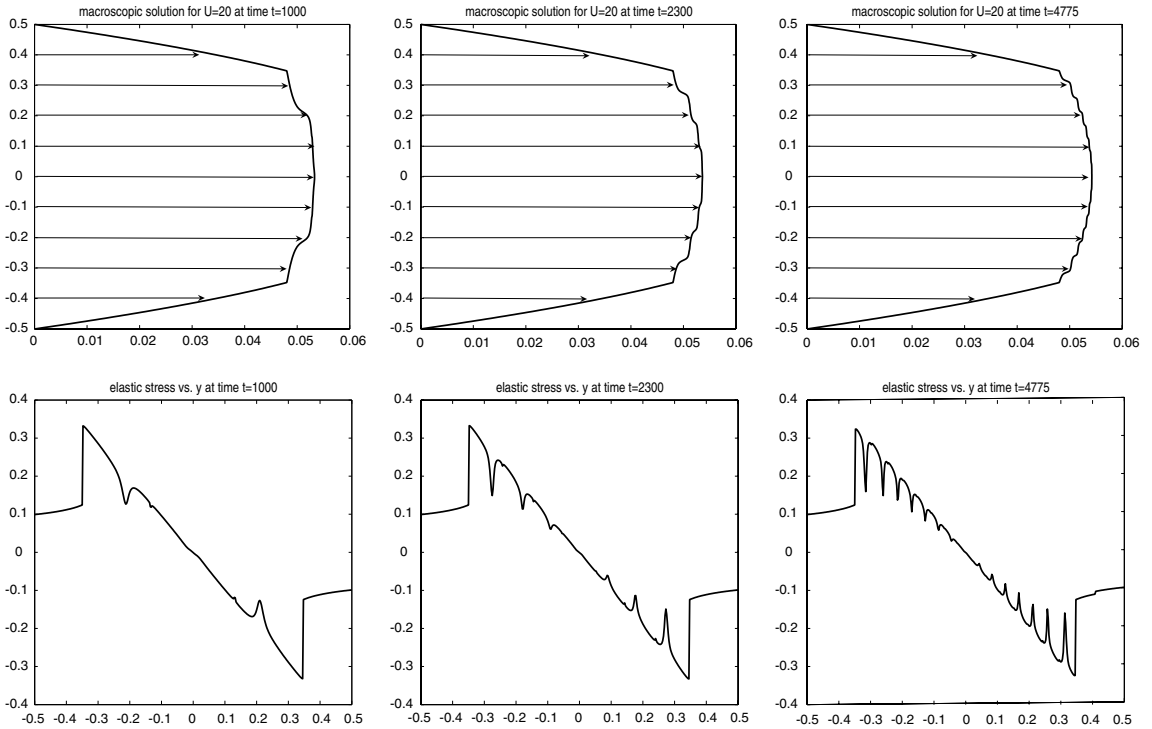

Fig. 10. Macroscopic velocity profile and elastic stress vs. y for Example 5.1 with $U = 20$ at different times (increasing from left to right).

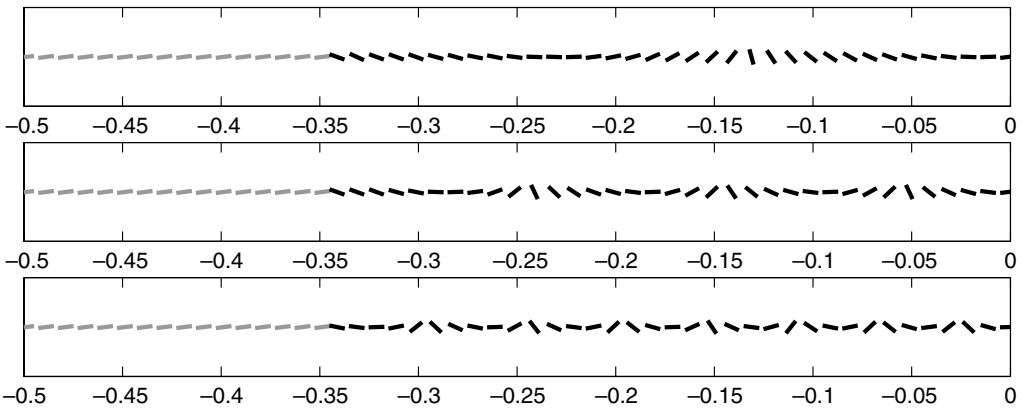

Fig. 11. Average orientation of rods over y (the half macroscopic domain) at different times corresponding to the plots of Fig. 10 (time is increasing from the top to the bottom). Horizontal rods are aligned with the flow direction, vertical rods with the shear direction. The light shaded part indicates the microscopic orientation inside the boundary layer and the dark shaded part indicates the microscopic orientation inside the bulk of the flow domain. The microscopic orientation is shown at every 4th grid point used to approximate the macroscopic solution structure.

6. Suspensions of rod-like molecules in a two-dimensional macroscopic flow

In this section, we generalize our numerical method to coupled flow problems in the dilute regime with general two-dimensional macroscopic velocity field of the form $\vec{u} = (u(x, y), v(x, y))$. Now the term $\vec{u} \cdot \nabla_{\vec{x}} \Psi$ of the Smoluchowski equation (2) which describes advection of the centers of mass by the macroscopic velocity does not drop out. The discretization of this term will be described in this section. The two-dimensional macroscopic flow equations were solved using the artificial compressibility method described in [25] on a finite difference grid as depicted in Fig. 12(b).

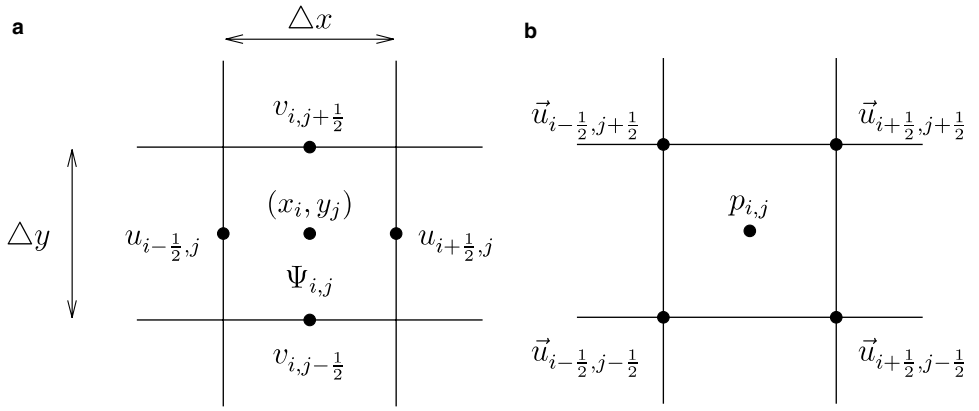

Fig. 12. (a) Specification of macroscopic velocities on finite volume grid for the discretization of Eq. (46). (b) Finite difference grid used for the discretization of the Stokes equation.

Assuming that an externally imposed macroscopic velocity field is given (which is the case during each time step of our method), we discretize the Smoluchowski equation (2) by solving the two subproblems

$$\partial_t \psi + \nabla_{\vec{n}} \cdot (P_{\vec{n}^\perp} \nabla_{\vec{x}} \vec{u} \vec{n} \psi) = D_r \nabla^2_{\vec{n}} \psi, \tag{45}$$

$$\partial_t \psi + \vec{u} \cdot \nabla_{\vec{x}} \psi = 0. \tag{46}$$

Our discretization of Eq. (45) has been explained in Section 3. Note that for a two-dimensional macroscopic flow problem subproblem (45) has to be solved for each grid cell of the two-dimensional macroscopic flow domain during each time step. Here it remains to describe the discretization of subproblem (46). We will use a high-resolution method for which the condition (1) remains satisfied at all times and at all discretization points in physical space, assuming that it is satisfied initially. Our numerical method is a variant of the high-resolution wave propagation algorithm, see [14,16]. Assume that the velocity at the intermediate time $t^{n+\frac{1}{2}}$ is specified at the midpoints of the cell interfaces of a finite volume grid, as shown in Fig. 12(a). In each grid cell, we require that the discrete divergence free condition

$$\frac{u_{i+\frac{1}{2},j} - u_{i-\frac{1}{2},j}}{\Delta x} + \frac{v_{i,j+\frac{1}{2}} - v_{i,j-\frac{1}{2}}}{\Delta y} = 0 \tag{47}$$

is satisfied. Let Ψ_{ij} denote the discrete description of the microscopic quantity ψ at the position (x_i, y_j) in physical space.

One time step of the finite volume method for Eq. (46) takes the form

$$\begin{aligned} \overline{\Psi}^{k,l}_{i,j} = \Psi^{k,l}_{i,j} &- \frac{\Delta t}{\Delta x}\left(\mathscr{A}^- \Delta \Psi^{k,l}_{i+\frac{1}{2},j} + \mathscr{A}^+ \Delta \Psi^{k,l}_{i-\frac{1}{2},j}\right) - \frac{\Delta t}{\Delta y}\left(\mathscr{A}^- \Delta \Psi^{k,l}_{i,j+\frac{1}{2}} + \mathscr{A}^+ \Delta \Psi^{k,l}_{i,j-\frac{1}{2}}\right) \\ &- \frac{\Delta t}{\Delta x}\left(\tilde{F}^{k,l}_{i+\frac{1}{2},j} - \tilde{F}^{k,l}_{i-\frac{1}{2},j}\right) - \frac{\Delta t}{\Delta y}\left(\tilde{G}^{k,l}_{i,j+\frac{1}{2}} - \tilde{G}^{k,l}_{i,j-\frac{1}{2}}\right) \quad \forall i,j,k,l, \end{aligned} \tag{48}$$

where $\mathscr{A}^\pm \Delta \Psi$ are first-order fluctuations and $\tilde{F}$, $\tilde{G}$ are high-resolution corrections. The first line in Eq. (48) represents the first-order update while the second line describes the second-order correction terms. The first-order fluctuations and second-order corrections in normal direction have the form

$$\mathscr{A}^\pm \Delta \Psi^{k,l}_{i-\frac{1}{2},j} := u^\pm_{i-\frac{1}{2},j}(\Psi^{k,l}_{i,j} - \Psi^{k,l}_{i-1,j}), \tag{49}$$

$$\mathscr{A}^\pm \Delta \Psi^{k,l}_{i,j-\frac{1}{2}} := v^\pm_{i,j-\frac{1}{2}}(\Psi^{k,l}_{i,j} - \Psi^{k,l}_{i,j-1}), \tag{50}$$

$$\tilde{F}^{k,l}_{i-\frac{1}{2},j} := \frac{1}{2}|u_{i-\frac{1}{2},j}|\left(1 - \frac{\Delta t}{\Delta x}|u_{i-\frac{1}{2},j}|\right)(\Psi^{k,l}_{i,j} - \Psi^{k,l}_{i-1,j})\lambda_{i-\frac{1}{2},j}, \tag{51}$$

$$\tilde{G}^{k,l}_{i,j-\frac{1}{2}} := \frac{1}{2}|v_{i,j-\frac{1}{2}}|\left(1 - \frac{\Delta t}{\Delta y}|v_{i,j-\frac{1}{2}}|\right)(\Psi^{k,l}_{i,j} - \Psi^{k,l}_{i,j-1})\lambda_{i,j-\frac{1}{2}}, \tag{52}$$

where λ is a total variation diminishing limiter, which may be applied in order to remove any non-physical oscillations introduced by the higher-order method. Furthermore $u^+ := \max(u,0)$ and $u^- := \min(u,0)$. In order to improve the accuracy and stability restrictions of this update, a transverse wave propagation, which eliminates the need of operator splitting must also be incorporated into the $\tilde{F}$ and $\tilde{G}$ terms, see [14–16]. The transverse propagation of the wave $\Psi^{k,l}_{i,j} - \Psi^{k,l}_{i-1,j}$ updates the $\tilde{G}$ fluxes in the form:

$$\begin{aligned}
\tilde{G}^{k,l}_{i-1,j-\frac{1}{2}} &:= \tilde{G}^{k,l}_{i-1,j\frac{1}{2}} - \frac{1}{2}\frac{\Delta t}{\Delta x} v^-_{i-1,j-\frac{1}{2}} u^-_{i-\frac{1}{2},j} (\Psi^{k,l}_{i,j} - \Psi^{k,l}_{i-1,j}),\\
\tilde{G}^{k,l}_{i-1,j+\frac{1}{2}} &:= \tilde{G}^{k,l}_{i-1,j+\frac{1}{2}} - \frac{1}{2}\frac{\Delta t}{\Delta x} v^+_{i-1,j+\frac{1}{2}} u^-_{i-\frac{1}{2},j} (\Psi^{k,l}_{i,j} - \Psi^{k,l}_{i-1,j}),\\
\tilde{G}_{i,j-\frac{1}{2}} &:= \tilde{G}_{i,j-\frac{1}{2}} - \frac{1}{2}\frac{\Delta t}{\Delta x} v^-_{i,j-\frac{1}{2}} u^+_{i-\frac{1}{2},j} (\Psi^{k,l}_{i,j} - \Psi^{k,l}_{i-1,j}),\\
\tilde{G}^{k,l}_{i,j+\frac{1}{2}} &:= \tilde{G}^{k,l}_{i,j+\frac{1}{2}} - \frac{1}{2}\frac{\Delta t}{\Delta x} v^+_{i,j+\frac{1}{2}} u^+_{i-\frac{1}{2},j} (\Psi^{k,l}_{i,j} - \Psi^{k,l}_{i-1,j}).
\end{aligned} \tag{53}$$

In addition, the differences $\Psi^{k,l}_{i,j} - \Psi^{k,l}_{i,j-1}$ change the $\tilde{F}$ fluxes in an analogous way.

It is easy to show that the first-order update of the wave propagation algorithm for the advective equation (46), under the assumption (47) is conservative. Since the second-order correction terms are formulated in flux difference form, formula (48) leads to a conservative update, i.e. our method is equivalent to a numerical method for the conservative equation

$$\partial_t \psi + \nabla_{\vec{x}} \cdot (\vec{u}\psi) = 0. \tag{54}$$

For our application we require that a discrete version of (1) is satisfied, i.e.

$$\sum_{k,l} \overline{\Psi}^{k,l}_{i,j} \sin(\theta_l) = 1 \quad \forall i,j \tag{55}$$

assuming that this relation is true for the microscopic solutions at the previous time step. For the method (48) with the fluctuations and correction terms as defined in (49)–(53), this relation can be verified easily. This is because all terms except the first term on the right-hand side of (48) contain differences of neighboring discrete values of Ψ. Note however that in order to satisfy (55) the wave limiters used in 51,52 should not depend on k,l.

A standard TVD wave limiter for this problem (compare with [16]) would depend on k and l in the form

$$\lambda^{k,l}_{i-\frac{1}{2},j} = \Lambda\left(\delta^{k,l}_{i-\frac{1}{2},j}\right), \quad \delta^{k,l}_{i-\frac{1}{2},j} := \frac{\Psi^{k,l}_{I,j} - \Psi^{k,l}_{I-1,j}}{\Psi^{k,l}_{i,j} - \Psi^{k,l}_{i-1,j}}, \quad I := \begin{cases} i-1 : u_{i-\frac{1}{2},j} > 0, \\ i+1 : u_{i-\frac{1}{2},j} < 0. \end{cases} \tag{56}$$

The minmod limiter, for instance, has the form

$$\Lambda(\delta) := \max(0, \min(1, \delta)). \tag{57}$$

In our application the condition (55) is satisfied only if the limiter used in (51) and (52) does not depend on k, l. This can be achieved by setting

$$\lambda_{i-\frac{1}{2},j} := \min_{k,l} \lambda^{k,l}_{i-\frac{1}{2},j}, \quad \lambda_{i,j-\frac{1}{2}} := \min \lambda^{k,l}_{i,j-\frac{1}{2}}, \tag{58}$$

i.e. we use a more restrictive limiter than needed to avoid nonphysical oscillations.

Since the high-resolution method (46) is explicit, a CFL condition must be imposed to ensure stability. The method requires

$$\max_{i,j}\left(\frac{\Delta t}{\Delta x}|u_{i-\frac{1}{2},j}|, \frac{\Delta t}{\Delta y}|v_{i,j-\frac{1}{2}}|\right) \leqslant 1. \tag{59}$$

6.1. Flow through a contracting channel

Here, we illustrate the performance of our numerical multiscale method in the dilute regime for a two-dimensional flow situation that has served as a widely used test case for numerical methods of macroscopic models (e.g. the Oldroyed B model), see for instance [26,30].

We approximate (2)–(5) in a channel with varying cross section, with a contraction ratio of 4:1. The channel is 16 units long and on the wider part 8 units high. At the inlet we impose parabolic Poiseuille flow

$$u(y) = \frac{3}{128}(16 - y^2), \quad v(y) = 0, \quad -4 \leqslant y \leqslant 4.$$

Outflow boundary conditions are used at the right boundary. At all other boundaries no-slip boundary conditions $\vec{u} = 0$ are imposed.

In Fig. 13, we show streamlines of the macroscopic steady-state solution. On the left-hand side we show the streamlines in the full geometry while on the right-hand side we show a close-up view of the vortex. The size of the vortex depends on D_r. This is in agreement to simulations for purely macroscopic models where a dependence of the size of the vortex on the Weissenberg number was observed.

6.2. Stability of spurt solutions

An interesting question that has so far not been explored for our coupled micro–macro system is the stability of one-dimensional spurt solutions in two space dimensions. In our last numerical test case, we want to illustrate that our numerical method may be able to reflect interesting stability behavior. Here we again

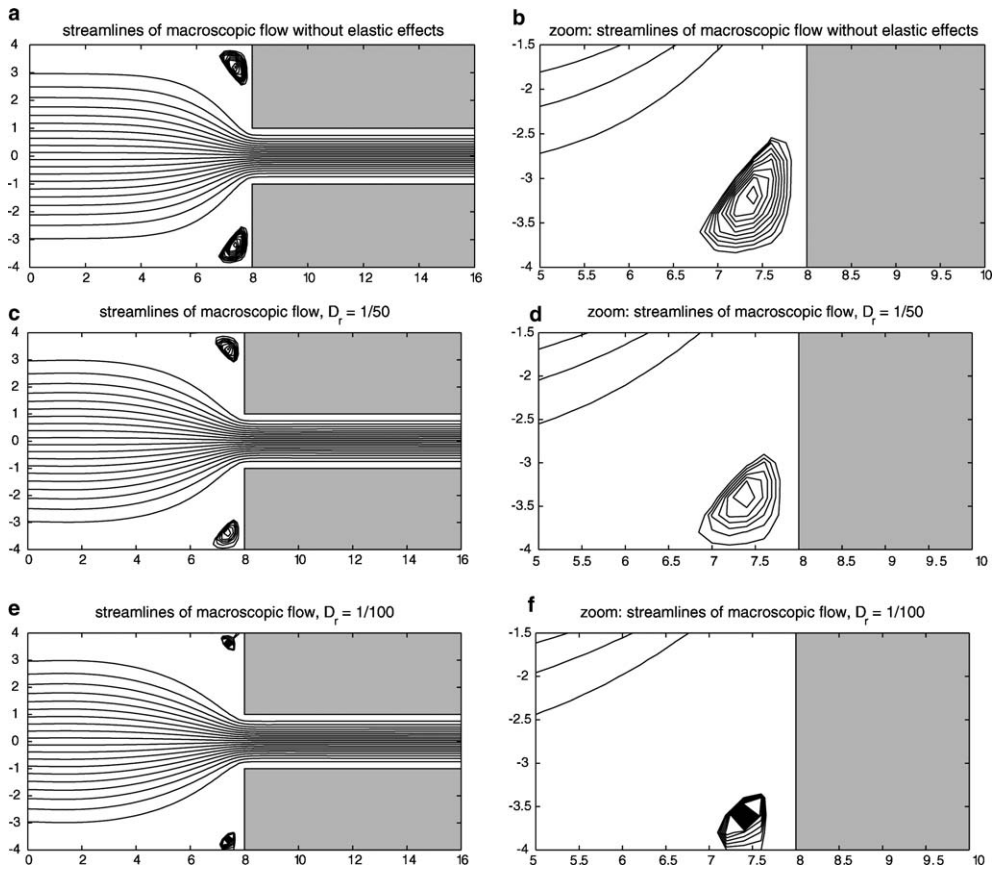

Fig. 13. Streamlines of the macroscopic flow through a contracting channel; (a,b) solution of Stokes equation without elastic effects, (c,d) solution of the micro–macro model for $D_r = 1/50$, (e,f) $D_r = 1/100$.

consider the dilute case. This stability test is motivated by work of Renardy [27], where the stability of a one-dimensionally stable spurt solution in two dimensions is investigated by linear stability analysis. There a Johnson–Segalman liquid was considered and it was found that the one-dimensionally stable spurt solutions are two-dimensionally unstable.

A two-dimensional spurt Couette flow is driven by the motion of the upper wall, which is here set to $u^{\text{top}} = 0.018$, $v^{\text{top}} = 0$, $u^{\text{bottom}} = v^{\text{bottom}} = 0$. The macroscopic physical domain is the rectangle $[0,2]\times[0,1]$. Periodic boundary conditions are used in the x-direction. In both the lower and the upper layer, we start our calculation with a steady-state microscopic solution ψ corresponding to a given velocity gradient of the form $\nabla_{\vec{x}}\vec{u}^{\text{ext}} = \begin{pmatrix} 0 & (u_y)^{1,2} \\ 0 & 0 \end{pmatrix}$ and the diffusion constant $D_{\text{r}} = 1/1000$. In the lower layer we use $(u_y)^1 = 0.005$ while in the upper layer $(u_y)^2 = 0.069$ is used. We add a perturbation to the position of the interface, i.e. the interface is initially located at $y = 0.8 + 0.01\sin(10\pi x)$, $x \in [0,2]$.

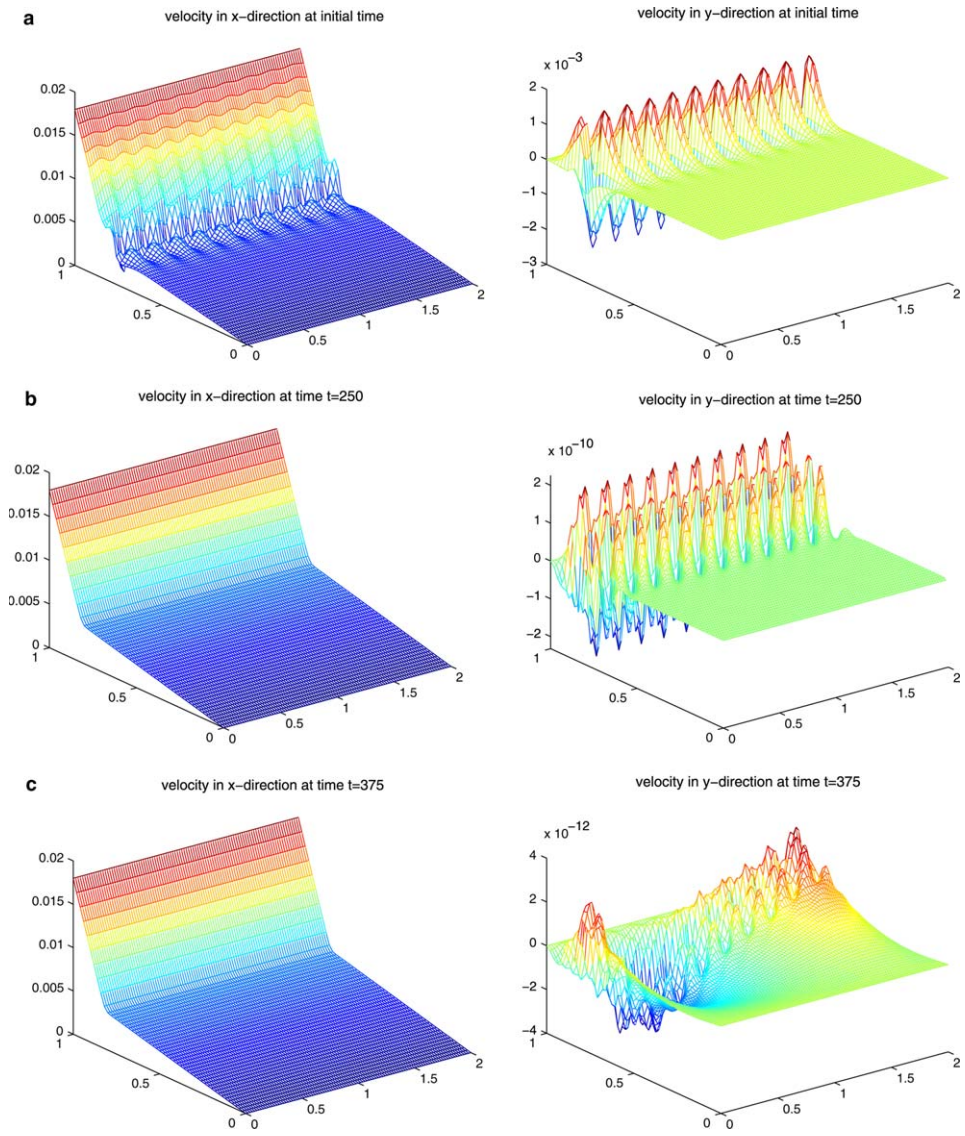

Fig. 14. Numerical investigation of the stability behavior of a one-dimensional spurt solution in two space dimensions.

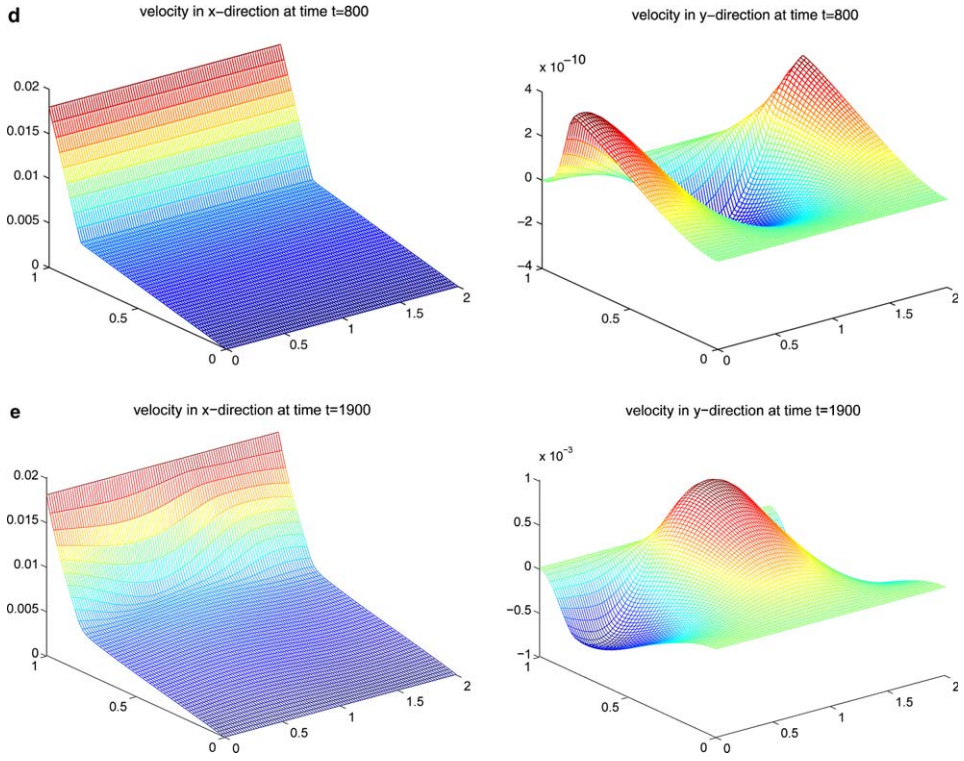

Fig. 14 (*continued*)

Fig. 14(a) shows the macroscopic velocity in the x and the y-direction at the initial time. The initial perturbation of the interface decreases, suggesting that the solution is stable to short-wave perturbations, see Fig. 14(b). The numerical results shown in Fig. 14(c)–(e) indicate that the solution is unstable for long or order one wave perturbations.

Acknowledgment

This work was supported by the German Science Foundation through SFB 611.

References

[1] J. Adams, P. Swarztrauber, R. Sweet, Fishpack: efficient fortran subprogram for the solution of separable elliptic partial differential equations. Available from: <http://www.scd.ucar.edu/css/software/fishpack/>.
[2] D.S. Bale, R.J. LeVeque, S. Mitran, J.A. Rossmanith, A wave propagation method for conservation laws and balance laws with spatially varying flux function, SIAM J. Sci. Comput. 24 (2002) 955–978.
[3] R.E. Bank, W.M. Coughran, W. Fichtner, E.H. Gross, D.J. Rose, R.K. Smith, Transient simulation of silicon devices and circuits, IEEE Trans. Comput. Aided Des. Integr.Circuits Syst. 4 (1985) 436–451.
[4] M. Doi, S.F. Edwards, The Theory of Polymer Dynamics, Oxford University Press, 1986.
[5] V. Fafaoni, M. Grosso, S. Crescitelli, P.L. Maffettone, The rigid–rod model for nematic polymers: an analysis of the shear flow problem, J. Rheol. 43 (1999) 829–843.
[6] D.D. Joseph, Fluid Dynamics of Viscoelastic Liquids, Springer, 1990.
[7] B. Jourdain, C. Le Bris, T. Leliévre, On a variance reduction technique for the micro–macro simulations of polymeric fluids, J. Non-Newtonian Fluid Mech. 122 (2004) 91–106.
[8] B. Jourdain, T. Leliévre, C. Le Bris, Numerical analysis of micro–macro simulations of polymeric fluid flows: A simple case, Math. Mod. Meth. Appl. S. 12 (2002) 1205–1243.
[9] R. Keunings, Micro–macro methods for the multiscale simulation of viscoelastic flow using molecular models of kinetic theory, Rheol. Rev. 2004, Brit. Soc. Rheol. (2004) 67–98.

[10] R.G. Larson, Arrested tumbling in shearing flows of liquid–crystal polymers, Macromolecules 23 (1990) 3983–3992.
[11] R.G. Larson, H.C. Öttinger, Effect of molecular elasticity on out-of-plane orientations in shearing flows of liquid crystalline polymers, Macromolecules 24 (1991) 6270–6282.
[12] M. Laso, H.C. Öttinger, Calculation of viscoelastic flow using molecular models: the CONNFFESSIT approach, J. Non-Newtonian Fluid Mech. 47 (1993) 1–20.
[13] R.J. LeVeque. CLAWPACK software. available from http://www.amath.washington.edu/~rjl/clawpack.html.
[14] R.J. LeVeque, High-resolution conservative algorithms for advection in incompressible flow, SIAM J. Numer. Anal. 33 (1996) 627–665.
[15] R.J. LeVeque, Wave propagation algorithms for multidimensional hyperbolic systems, J. Comput. Phys. 131 (1997) 327–353.
[16] R.J. LeVeque, Finite Volume Methods for Hyperbolic Problems, Cambridge University Press, 2002.
[17] R.J. LeVeque, The dynamics of pressureless dust clouds and delta waves, J. Hyperbolic Differential Equations 1 (2004) 315–327.
[18] D.S. Malkus, J.A. Nohel, B.J. Plohr, Analysis of the spurt phenomena for a non-Newtonian fluid, Lect. Notes Phys. 359 (1990) 112–132.
[19] D.S. Malkus, J.A. Nohel, B.J. Plohr, Dynamics of shear-flow of a non-Newtonian fluid, J. Comput. Phys. 87 (1990) 464–487.
[20] D.S. Malkus, J.A. Nohel, B.J. Plohr, Analysis of new phenomena in shear-flow of non-Newtonian fluids, SIAM J. Appl. Math. 51 (1991) 899–929.
[21] G. Marrucci, P.L. Maffettone, Description of the liquid-crystalline phase of rodlike polymers at high shear rates, Macromolecules 22 (1989) 4076–4082.
[22] J.A. Nohel, R.L. Pego, On the generation of discontinuous shearing motions of a non-Newtonian fluid, Arch. Rat. Mech. Anal. 139 (1997) 355–376.
[23] J.A. Nohel, R.L. Pego, A.E. Tzavaras, Stability of discontinuous steady states in shearing motions of a non-Newtonian fluid, Proc. Roy. Soc. Edinb. 115A (1990) 39–59.
[24] F. Otto, A.E. Tzavaras, Continuity of velocity gradients in suspensions of rod-like molecules, 2004. SFB 611 Preprint, Nr. 141.
[25] R. Peyret, T.D. Taylor, Computational Methods for Fluid Flow, Springer, 1983.
[26] T.N. Phillips, A.J. Williams, Comparison of creeping and inertial flow of an Oldroyd B fluid through planar and axisymmetric contractions, J. Non-Newtonian Fluid Mech. 108 (2002) 25–47.
[27] Y.Y. Renardy, Spurt and instability in a two-layer Johnson–Segalman liquid, Theoret. Comput. Fluid Dynamics 7 (1995) 463–475.
[28] J.A. Rossmanith, A wave propagation method for hyperbolic systems on the sphere, J. Comput. Phys., in press, doi:10.1016/j.jcp.2005.08.027.
[29] G. Strang, On the construction and comparison of difference schemes, SIAM J. Num. Anal. 5 (1968) 506–517.
[30] D. Trebotisch, P. Colella, G.H. Miller, A stable and convergent scheme for viscoelastic flow in contraction channels, J. Comput. Phys. 205 (2005) 315–342.
[31] G. Vinogradov, A. Malkin, Y. Yanovskii, E. Borisenkova, B. Yarlykov, G. Berezhnaya, Viscoelastic properties and flow of narrow distribution polybutadienes and polyisoprenes, J. Polymer Sci. Part A-2 10 (1972) 577–596.